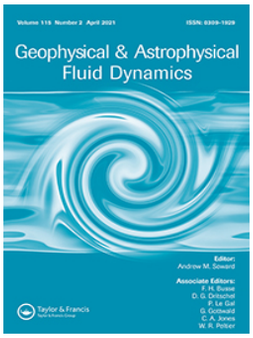

Geophysical & Astrophysical Fluid Dynamics

ISSN: (Print) (Online) Journal homepage: https://www.tandfonline.com/loi/ggaf20

Thermal versus isothermal rotating shallow water equations: comparison of dynamical processes by simulations with a novel well-balanced central-upwind scheme

Alexander Kurganov, Yongle Liu & Vladimir Zeitlin

To cite this article: Alexander Kurganov, Yongle Liu & Vladimir Zeitlin (2021) Thermal versus isothermal rotating shallow water equations: comparison of dynamical processes by simulations with a novel well-balanced central-upwind scheme, Geophysical & Astrophysical Fluid Dynamics, 115:2, 125-154, DOI: 10.1080/03091929.2020.1774876

To link to this article: https://doi.org/10.1080/03091929.2020.1774876

Published online: 15 Jun 2020.

GEOPHYSICAL & ASTROPHYSICAL FLUID DYNAMICS
2021, VOL. 115, NO. 2, 125–154
https://doi.org/10.1080/03091929.2020.1774876

Taylor & Francis
Taylor & Francis Group

Thermal versus isothermal rotating shallow water equations: comparison of dynamical processes by simulations with a novel well-balanced central-upwind scheme

Alexander Kurganov[a,b], Yongle Liu [a,c] and Vladimir Zeitlin[a,d]

[a]Department of Mathematics, Southern University of Science and Technology, Shenzhen, People's Republic of China; [b]SUSTech International Center for Mathematics, Southern University of Science and Technology, Shenzhen, People's Republic of China; [c]Department of Mathematics, Harbin Institute of Technology, Harbin, People's Republic of China; [d]Laboratory of Dynamical Meteorology, Sorbonne University (SU), Paris, France

ABSTRACT

We introduce a new high-resolution well-balanced central-upwind scheme for two-dimensional rotating shallow water equations with horizontal temperature/density gradients – thermal rotating shallow water equations. The scheme maintains the equilibrium states in the presence of topography and temperature/density variations, and allows for high-resolution tracking of the active scalar field together with velocity and pressure fields. We use the new scheme to highlight both the similarities and differences in the predictions of the thermal and isothermal shallow water models for the fundamental dynamical processes: evolution of isolated vortices in the midlatitude β-plane in the presence of topography and relaxation of localised pressure and temperature perturbations in the equatorial β-plane.

ARTICLE HISTORY
Received 9 March 2020
Accepted 24 May 2020

KEYWORDS
Thermal rotating shallow water equations; vortex dynamics; equatorial waves; central-upwind scheme

1. Introduction

Rotating shallow water (RSW) equations, in spite of their simplicity, capture essential features of the dynamics of large-scale motions in the atmosphere and oceans, and allow for efficient and computationally low-cost modelling. Major dynamical phenomena can be understood with this model (Zeitlin 2018), in particular large-scale vortex and wave dynamics. However, an important element is lacking in the the RSW model, as it does not allow for gradients of the mean temperature and/or density, which are ubiquitous in the atmosphere and oceans. In particular, in the context of vortex dynamics, oceanic eddies are typically warm- or cold-core (see, e.g. Sun *et al.* 2019), and archetypal atmospheric vortices, the tropical storms, are warm-core (see, e.g. Halverson *et al.* 2006). An improved in this respect thermal rotating shallow water (TRSW) model was multiply reinvented both in the meteorological and oceanographic literature, in the context of the boundary layer in the atmosphere (Lavoie 1972, Salby 1989), and of the mixed layer in the ocean

CONTACT Yongle Liu liuyl2017@mail.sustech.edu.cn

(McCreary *et al.* 1993, Young 1994, Ripa 1995). More recently, it was applied to planetary atmospheres (Cho *et al.* 2008, Warnerford and Dellar 2014), and was rediscovered again in the context of testing the general circulation models (Zerroukat and Allen 2015). The TRSW model has some specific properties which will be addressed below. These properties will be highlighted with the help of a new high-resolution well-balanced central-upwind scheme, which is derived in this paper. To the best of our knowledge, this is the first well-balanced scheme (in the sense that it is capable of preserving on the discrete level thermo-geostrophic equilibria) for the TRSW equations. In the absence of rotation, well-balanced schemes for thermal shallow water equations have been recently developed by Chertock *et al.* (2014) and Sánchez-Linares *et al.* (2016). The importance of well-balanced numerical schemes is obvious, as large-scale dynamical features in the atmosphere and ocean are usually close to the geostrophic equilibrium and usually evolve in the presence of non-flat bathymetry/topography. Adequate numerical schemes should be also able to resolve sharp temperature fronts, since a description of such fronts was part of the initial motivation to introduce this type of models (see, e.g. Dempsey and Rotunno 1988, Young and Chen 1995).

Recently, we have proposed and successfully tested a well-balanced central-upwind scheme for the one-dimensional (1D) version of the TRSW model, in fact, the "one-and-a-half" dimensional as, due to rotation, both components of velocity should be present even if there is no dependence on one of the spatial coordinates (see Kurganov *et al.* 2020). The scheme is derived using the flux globalisation approach originally proposed in Chertock *et al.* (2018c) and then used for the Saint-Venant system of shallow water equations with Manning friction terms (Cheng *et al.* 2019) and Euler equations of gas dynamics with gravitation (Chertock *et al.* 2018a). In this approach, the source terms are incorporated into the fluxes, which become global. The obtained system of conservation laws with global fluxes is then numerically solved using the Riemann-problem-solver-free central-upwind scheme, which was derived for general multidimensional hyperbolic systems of conservation laws in a series of works (see, e.g. Kurganov and Tadmor 2000, Kurganov *et al.* 2001, Kurganov and Tadmor 2002, Kurganov and Lin 2007, Kurganov 2016). The resulting method is guaranteed to be well-balanced thanks to the reconstruction of equilibrium variables, which is needed in order to construct a high-order scheme, and special well-balanced evolution (in some of the numerical flux components, a part of the numerical diffusion is switched off when the solution is at or near the equilibrium).

In this paper, we show how the above-cited method can be generalised to the full two-dimensional (2D) model, and use it to determine differences and new elements appearing in TRSW, as compared to the "ordinary" RSW model, in the representation of fundamental dynamical processes: evolution of the isolated vortices on the mid-latitude β-plane and relaxation of localised perturbations on the equatorial β-plane. Our paper is organised as follows. In section 2, we introduce the model and describe its basic properties. In section 3, we sketch the numerical method, the details being relegated to the Appendices A and B. In section 4, we present the results of the comparative analysis of the evolution of localised vortices on the mid-latitude β-plane with a non-flat bottom topography in the TRSW and RSW models. In section 5, we give the results of the comparative analysis of the relaxation (adjustment) of localised pressure and temperature anomalies on the equatorial β-plane. Finally, section 6 contains brief conclusions.

2. TRSW model and its fundamental properties

2.1. Equations of the model and their interpretation

The equations of the model, in the absence of dissipation, are written for the horizontal velocity $\boldsymbol{v}(x, y, t) = (u(x, y, t), v(x, y, t))$, the thickness of the fluid layer $h(x, y, t)$, and the field $b(x, y, t)$ related to temperature/density variations

$$\boldsymbol{v}_t + \boldsymbol{v}\cdot\nabla\boldsymbol{v} + f(y)\hat{\boldsymbol{z}} \wedge \boldsymbol{v} = -b\nabla(h + Z) - \tfrac{1}{2}h\nabla b, \tag{1a}$$

$$h_t + \nabla\cdot(\boldsymbol{v}h) = 0, \tag{1b}$$

$$b_t + \boldsymbol{v}\cdot\nabla b = 0. \tag{1c}$$

Here, x and y are spatial variables, t is the time, $Z(x, y)$ is the bottom topography, $\nabla := (\partial/\partial x, \partial/\partial y)$, $\hat{\boldsymbol{z}}$ is the unit vector in the vertical direction, and $f(y) = f_0 + \beta y$ is the Coriolis parameter in the β-plane approximation.

These equations hold both in the oceanic and atmospheric contexts, b being related to the density anomaly in the former case and to the potential temperature anomaly in the latter case. The model can be derived by vertical averaging of the primitive equations under the columnar motion hypothesis, like the standard RSW equations which arise from (1) in the limit of constant b, with the only difference in the derivation consisting in relaxation of the hypothesis of constant mean density (Chapter 14 Zeitlin 2018). We would like to emphasise that the physical meaning of b depends on the interpretation of the TRSW model. In the oceanic context, if the model is understood as purely barotropic and is obtained by vertical averaging through the whole depth (as in Zeitlin 2018), then $b = g\rho/\rho_0$, where ρ and ρ_0 are the variable and constant parts of the water density, respectively. This means that b is a decreasing function of height. If the model is understood as describing the baroclinic motions in the two-layer ocean with an infinitely deep lower layer (as in Warneford and Dellar 2013), then $b = g(\rho_0 - \rho)/\rho_0$, where ρ and $\rho_0 =$ Const are densities of the upper and lower layers, that is, b is an increasing function of height. However, introducing the non-flat bottom topography with such interpretation does not make much sense. In the atmospheric context, the density ρ should be replaced with the potential temperature θ, and the fluid layer is upside-down, with the free surface at the ground, and pseudo-height used as the vertical coordinate (Zeitlin 2018).

Before moving forward, let us recall a crucial observation made by Gouzien *et al.* (2017). It is well-known that the standard RSW model is equivalent to the compressible Euler equations for rotating isentropic gas with density h and the equation of state $P = gh^2/2$ for pressure P. Similarly, the TRSW model (1) can be interpreted as dynamics of a compressible gas under the influence of the Coriolis force with density h, entropy b, and the equation of state $P = bh^2/2$. An additional observation is that the latter becomes the standard equation of state of a polytropic gas with polytropic index 2, density h, and entropy s under the change of variable $b = \mathrm{e}^s$ (under this change the equation of advection of b reduces to the equation of advection of s). It should be pointed out that the potential temperature θ has precisely the required expression in terms of entropy: $\theta = \mathrm{e}^s$. This interpretation shows the internal consistency of the model in spite of its unusual properties to be discussed below.

2.2. Conservation laws, forcing and dissipation

An important difference between the TRSW and standard RSW model is that the potential vorticity (PV) $Q = (\zeta + f)/h$, where $\zeta = v_x - u_y$ is the relative vorticity, is not a Lagrangian invariant of the system (1) as follows from the direct calculation

$$\frac{\mathrm{d}Q}{\mathrm{d}t} = Q_t + \boldsymbol{v}\cdot\nabla Q = \frac{1}{h}\left[\left(\frac{h}{2}+Z\right)_x b_y - \left(\frac{h}{2}+Z\right)_y b_x\right] = \frac{1}{h}\mathcal{J}\left(\frac{h}{2}+Z, b\right),$$

where $\mathcal{J}(\phi,\psi) := \phi_x\psi_y - \phi_y\psi_x$ is the 2D Jacobian. Instead, a global conservation law for the PV integrated over a domain S_b, delimited by an advected isentrope $b = \text{const.}$, can be established (Warneford and Dellar 2013), namely

$$\frac{\mathrm{d}}{\mathrm{d}t}\int_{S_b} hQ\,\mathrm{d}x\,\mathrm{d}y = 0. \tag{2}$$

One could be surprised by the apparent violation of the Ertel potential vorticity theorem, especially in view of the above interpretation of the TRSW model as polytropic gas dynamics. The resolution of this paradox is simple: while in the Ertel general potential vorticity formula, the vorticity is projected onto the gradient of entropy, in the present quasi 2D model they are orthogonal (the vorticity is vertical and the gradients of b are horizontal).

It follows from (1) that the buoyancy is a Lagrangian invariant and the mass is locally conserved. As usual, combining the first two equations gives a local momentum conservation, while combining the last two equations gives a local conservation of the buoyancy integrated over the layer hb (recall that b is the average buoyancy of the layer). In this way we arrive at the equations of motion in the form of balance laws, which would be conservation laws in the absence of rotation and bottom topography. They are

$$h_t + (hu)_x + (hv)_y = 0, \tag{3a}$$

$$q_t + \left(hu^2 + \tfrac{1}{2}bh^2\right)_x + (huv)_y = fp - hbZ_x, \tag{3b}$$

$$p_t + (huv)_x + \left(hv^2 + \tfrac{1}{2}bh^2\right)_y = -fq - hbZ_y, \tag{3c}$$

$$(hb)_t + (hub)_x + (hvb)_y = 0, \tag{3d}$$

where $q := hu$ and $p := hv$ are zonal and meridional momentum densities, respectively. These balance laws will be used for constructing the numerical scheme presented below.

It is easy to check that the total energy of the system, which is the sum of the kinetic and potential energies,

$$E = \int_{-\infty}^{\infty}\left[h\left(\frac{u^2+v^2}{2}\right) + \frac{b(h+Z)^2}{2}\right]\mathrm{d}x\,\mathrm{d}y$$

is conserved.

For the purposes of modelling specific oceanic and atmospheric phenomena, the momentum equations (3b) and (3c) can be subject to body forces and the entropy conservation equation (3c) can be subject to diabatic cooling/heating. Apart from molecular viscosity and diffusion, which can be introduced in a standard way on the right-hand sides of (3a-d) as being proportional to the Laplacians of the corresponding quantities, a bottom

drag of the form $-K(|\boldsymbol{v}|)q$ and $-K(|\boldsymbol{v}|)p$ can be introduced on the right-hand side of (3b) and (3c), and diabatic relaxation to an equilibrium potential temperature distribution of the form $-(h/\tau)(\theta-\theta_e)$ can be added on the right-hand side of (3d), when θ replaces b in atmospheric applications.

2.3. The thermo-(cyclo)geostrophic equilibrium and quasi-geostrophic approximation

It is of common knowledge that Coriolis and pressure forces are usually approximately balanced in large-scale atmospheric and oceanic motions. This is the geostrophic balance. Written in terms of the gas dynamics analogy explained above it looks rather standard, but if expressed in terms of the original variables, it becomes unusual compared with the standard RSW model

$$f\hat{\boldsymbol{z}}\wedge\boldsymbol{v}=-h^{-1}\nabla P=-h^{-1}\nabla\left(\tfrac{1}{2}bh^2\right)=-b\nabla h-\tfrac{1}{2}h\nabla b. \tag{4}$$

This is the *thermo-geostrophic balance* (Gouzien *et al.* 2017) which means that the same velocity distribution can be obtained either by pure "normal" hydrostatic pressure gradient at constant b (*geostrophic balance*), by pure buoyancy (temperature) gradient at constant h (*thermal balance*), or by a combination of both. In order to understand the meaning of this fact and an apparent contradiction with the classical notion of the thermal wind, as in the case of thermal balance we have a horizontal density/temperature gradient and no vertical shear of velocity, we should recall that the TRSW model is derived by vertically averaging the primitive equations. By construction, the vertical shear is averaged out in the resulting TRSW equations, leaving only the mean. Therefore, the thermal balance between the Coriolis and density/temperature gradient terms can be understood as vertically averaged thermal wind balance, and an admixture of "thermal" balance in the "normal" geostrophic balance in (4) can be interpreted as a proxy for the baroclinicity of the mean flow. In this terms, one can understand a surprising instability of the plane-parallel flow maintained by an across-flow temperature gradient (see, e.g. Zeitlin 2018), which was already reported in the early papers as a proxy of the classical symmetric instability (Stone 1966).

In what follows, we will be using axisymmetric stationary vortex solutions of the system (1) on the f-plane, that is, with $f(y)\equiv f_0=$ const., with zero radial velocity, azimuthal velocity V, thickness h and buoyancy b as functions of the radial coordinate r only. After rewriting (1) in polar coordinates, it is easy to see that in order to provide an exact solution, these fields should be in *thermo-cyclogeostrophic equilibrium*

$$r^{-1}V^2(r)+f_0V(r)=b(r)h'(r)+\tfrac{1}{2}b'(r)h(r). \tag{5}$$

A given velocity profile $V(r)$ can be, thus, obtained by adjusting the profile $h(r)$ with flat b ("normal" vortex), or by adjusting the profile $b(r)$ with flat h ("thermal" vortex), or with non-trivial profiles for both h and b ("mixed" vortex) (see Gouzien *et al.* 2017).

Quasi-geostrophic (QG) approximation of the TRSW equations, see (Warneford and Dellar 2013), can be obtained along the same lines as in the standard RSW case. Considering fluid motions with a typical spatial and velocity scales L_s and U, respectively, and introducing unperturbed thickness H_0 and reference buoyancy B_0, we define in a standard

way the Rossby and Burger numbers,

$$Ro = \frac{U}{f_0 L_s} \qquad \text{and} \qquad Bu = \frac{B_0 H_0}{f_0^2 L_s^2} \equiv \frac{R_d^2}{L_s^2},$$

respectively. Here, R_d denotes the deformation radius. We then put ourselves in the QG regime by supposing $Bu = \mathrm{O}(1)$, $Ro \ll 1$, and using the following scaling

$$x = L_s\widetilde{x}, \qquad t = (L_s/U)\,\widetilde{t}, \qquad u = U\widetilde{u}, \qquad v = U\widetilde{v}, \tag{6a–d}$$

$$h = H_0\big(1 + (Ro/Bu)\eta\big), \qquad b = B_0\big(1 + 2(Ro/Bu)\theta\big), \tag{6e,f}$$

where $\widetilde{x}$, $\widetilde{t}$, $\widetilde{u}$, $\widetilde{v}$, η and θ are the non-dimensional variables and $\eta(r)$ and $\theta(r)$ represent deviations from the values of respective fields at infinity.

We then substitute (6) into (4) and obtain in the leading order in Ro (for simplicity, we take $Bu = 1$, and assume, as usual in the QG regime, that non-dimensional meridional gradient of the Coriolis parameter β is of the order of Ro)

$$\hat{\boldsymbol{z}} \wedge \boldsymbol{v} = -\nabla(\eta + \theta) = -\nabla\psi,$$

where $\psi := \eta + \theta$ is the geostrophic streamfunction. At the next order, we obtain

$$\big(\nabla^2\psi - \psi + \theta\big)_t + \mathcal{J}(\psi, \nabla^2\psi) + \psi_x = 0, \tag{7a}$$

$$\theta_t + \mathcal{J}(\psi, \theta) = 0. \tag{7b}$$

Simultaneously, using the scaling (6), we can rewrite the thermo-cyclogeostrophic equilibrium (5) in non-dimensional variables as

$$\left(1 + Ro\frac{V(r)}{r}\right) V(r) = \left(1 + 2\frac{Ro}{Bu}\theta(r)\right)\eta'(r) + \left(1 + \frac{Ro}{Bu}\eta(r)\right)\theta'(r). \tag{8}$$

3. Well-balanced semi-discrete central-upwind scheme for two-dimensional TRSW equations

Solving the TRSW system (3) numerically is quite challenging. First, the solutions of this hyperbolic system of balance laws admit non-smooth solutions and therefore one needs to develop a shock-capturing scheme. In the absence of rotation and topography, existence of shocks becomes obvious already from the gas dynamics analogy explained in section 2.1. The Rankine-Hugoniot conditions across a shock moving in the x-direction with velocity C in such system readily follow from (3)

$$-C[h] + [hu] = 0, \tag{9a}$$

$$-C[hu] + \big[hu^2 + \tfrac{1}{2}bh^2\big] = 0, \tag{9b}$$

$$-C[hb] + [hub] = 0, \tag{9c}$$

where, here and only here, square brackets denote, as usual, a jump of the corresponding quantity across the shock. Existence of shocks in the presence of rotation was demonstrated

in the model of Kurganov *et al.* (2020). Second, a delicate balance between the flux and source terms should be maintained in order to be able to capture small perturbations of physically relevant thermo-geostrophic equilibria on practically affordable and thus reasonably coarse grids. Therefore, one needs to develop a well-balanced scheme, which is capable of exactly preserving two particular thermo-geostrophic equilibria, the so-called jets in the rotating frame,

$$q \equiv 0, \qquad p_y \equiv 0, \qquad h_y \equiv 0, \qquad b_y \equiv 0, \qquad Z_y \equiv 0, \qquad K \equiv \text{const.}$$

and

$$p \equiv 0, \qquad q_x \equiv 0, \qquad h_x \equiv 0, \qquad b_x \equiv 0, \qquad Z_x \equiv 0, \qquad L \equiv \text{const.},$$

where K and L are global quantities defined below in (12), on a discrete level. This can be achieved using a flux globalisation approach originally proposed by Chertock *et al.* (2018c).

Following Chertock *et al.* (2018a, 2018c) and Cheng *et al.* (2019), we first incorporate the source terms into the fluxes and rewrite the system (3) in the following equivalent form

$$\boldsymbol{U}_t + \boldsymbol{F}(\boldsymbol{U}, Z)_x + \boldsymbol{G}(\boldsymbol{U}, Z)_y = \boldsymbol{0}, \tag{10}$$

where

$$\boldsymbol{U} = \begin{pmatrix} h \\ q \\ p \\ hb \end{pmatrix}, \qquad \boldsymbol{F}(\boldsymbol{U}, Z) = \begin{pmatrix} q \\ K \\ pq/h \\ qb \end{pmatrix}, \qquad \boldsymbol{G}(\boldsymbol{U}, Z) = \begin{pmatrix} p \\ pq/h \\ L \\ pb \end{pmatrix}, \tag{11a–c}$$

and K and L are global fluxes given by

$$K = hu^2 + \frac{b}{2}h^2 - \int^x \Big[f(y)p(\xi, y, t) - h(\xi, y, t)b(\xi, y, t)Z_x(\xi, y)\Big]\mathrm{d}\xi, \tag{12a}$$

$$L = hv^2 + \frac{b}{2}h^2 + \int^y \Big[f(\xi)q(x, \xi, t) + h(x, \xi, t)b(x, \xi, t)Z_y(x, \xi)\Big]\mathrm{d}\xi, \tag{12b}$$

where the integrals represent the anti-derivatives with respect of x and y, respectively.

The system (10)–(12) is a hyperbolic system of conservation laws with global fluxes, which makes it hard to develop upwind schemes, which are based on (approximately) solving (generalised) Riemann problems. We therefore apply the 2D semi-discrete second-order central-upwind scheme to the system (10)–(12). Central-upwind schemes belong to the class of Riemann-problem-solver-free Godunov-type non-oscillatory central schemes (see, e.g. Kurganov 2016). A special version of the central-upwind schemes for systems obtained using the flux globalisation approach was proposed by Chertock *et al.* (2018a) in the context of Euler equations of gas dynamics with gravitation and then improved by Kurganov *et al.* (2019), where the numerical dissipation switch was introduced. The central-upwind scheme for the 1D version of the TRSW system has been recently introduced by Kurganov *et al.* (2020).

In this section, we briefly describe a well-balanced semi-discrete second-order central-upwind scheme for the 2D TRSW system (3). To this end, we use a Cartesian mesh with

the uniform cells $C_{j,k} := [x_{j-\frac{1}{2}}, x_{j+\frac{1}{2}}] \times [y_{k-\frac{1}{2}}, y_{k+\frac{1}{2}}]$ of size $|C_{j,k}| = \Delta x \Delta y$, and denote the discrete solutions by its computed cell averages

$$\overline{\boldsymbol{U}}_{j,k}(t) :\approx \frac{1}{\Delta x \Delta y} \iint_{C_{j,k}} \boldsymbol{U}(x,y,t)\,\mathrm{d}x\,\mathrm{d}y,$$

which are assumed to be available at a certain time t. These cell averages are evolved in time using the following semi-discretisation

$$\frac{\mathrm{d}}{\mathrm{d}t}\,\overline{\boldsymbol{U}}_{j,k}(t) = -\frac{\mathcal{F}_{j+\frac{1}{2},k}(t) - \mathcal{F}_{j-\frac{1}{2},k}(t)}{\Delta x} - \frac{\mathcal{G}_{j,k+\frac{1}{2}}(t) - \mathcal{G}_{j,k-\frac{1}{2}}(t)}{\Delta y}, \tag{13}$$

where $\mathcal{F}_{j+\frac{1}{2},k}(t)$ and $\mathcal{G}_{j,k+\frac{1}{2}}(t)$ are the central-upwind numerical fluxes, which depend on the reconstructed point values of $\boldsymbol{U}$ at the cell interfaces and one-sided local speeds of propagation.

The point values are reconstructed using a piecewise linear interpolant and they are denoted by

$$\begin{aligned} \boldsymbol{U}^{\mathrm{E}}_{j,k} &\approx \boldsymbol{U}(x_{j+\frac{1}{2}}, y_k), & \boldsymbol{U}^{\mathrm{W}}_{j,k} &\approx \boldsymbol{U}(x_{j-\frac{1}{2}}, y_k),\\ \boldsymbol{U}^{\mathrm{N}}_{j,k} &\approx \boldsymbol{U}(x_j, y_{k+\frac{1}{2}}), & \boldsymbol{U}^{\mathrm{S}}_{j,k} &\approx \boldsymbol{U}(x_j, y_{k-\frac{1}{2}}). \end{aligned}$$

The details on the reconstruction are provided in Appendix 1. An important ingredient of the new method which we present here, relegating all other details to the Appendix 2, are the one-sided local speeds of propagation in the x- and y-directions. They are obtained using the eigenvalues of the corresponding Jacobians $\partial \boldsymbol{F}/\partial \boldsymbol{U}$ and $\partial \boldsymbol{G}/\partial \boldsymbol{U}$ with the modification that switches off a part of the numerical dissipation near contact discontinuities and shears

$$a^+_{j+\frac{1}{2},k} = \max\left\{u^{\mathrm{E}}_{j,k} + \alpha_{j+\frac{1}{2},k}\sqrt{h^{\mathrm{E}}_{j,k} b^{\mathrm{E}}_{j,k}},\, u^{\mathrm{W}}_{j+1,k} + \alpha_{j+\frac{1}{2},k}\sqrt{h^{\mathrm{W}}_{j+1,k} b^{\mathrm{W}}_{j+1,k}},\, 0\right\}, \tag{14a}$$

$$a^-_{j+\frac{1}{2},k} = \min\left\{u^{\mathrm{E}}_{j,k} - \alpha_{j+\frac{1}{2},k}\sqrt{h^{\mathrm{E}}_{j,k} b^{\mathrm{E}}_{j,k}},\, u^{\mathrm{W}}_{j+1,k} - \alpha_{j+\frac{1}{2},k}\sqrt{h^{\mathrm{W}}_{j+1,k} b^{\mathrm{W}}_{j+1,k}},\, 0\right\}, \tag{14b}$$

$$a^+_{j,k+\frac{1}{2}} = \max\left\{v^{\mathrm{N}}_{j,k} + \alpha_{j,k+\frac{1}{2}}\sqrt{h^{\mathrm{N}}_{j,k} b^{\mathrm{N}}_{j,k}},\, v^{\mathrm{S}}_{j,k+1} + \alpha_{j,k+\frac{1}{2}}\sqrt{h^{\mathrm{S}}_{j,k+1} b^{\mathrm{S}}_{j,k+1}},\, 0\right\}, \tag{14c}$$

$$a^-_{j,k+\frac{1}{2}} = \min\left\{v^{\mathrm{N}}_{j,k} - \alpha_{j,k+\frac{1}{2}}\sqrt{h^{\mathrm{N}}_{j,k} b^{\mathrm{N}}_{j,k}},\, v^{\mathrm{S}}_{j,k+1} - \alpha_{j,k+\frac{1}{2}}\sqrt{h^{\mathrm{S}}_{j,k+1} b^{\mathrm{S}}_{j,k+1}},\, 0\right\}. \tag{14d}$$

Here, $\alpha_{j+\frac{1}{2},k} \in [0,1]$ and $\alpha_{j,k+\frac{1}{2}} \in [0,1]$ are the switch parameters, which are computed as follows

$$\alpha_{j+\frac{1}{2},k} = \begin{cases} \Delta\alpha^{(1)}_{j+\frac{1}{2},k} \Big/ \Delta\alpha_{j+\frac{1}{2},k}, & \text{if } \Delta\alpha_{j+\frac{1}{2},k} > \nu,\\ 0, & \text{otherwise,} \end{cases} \tag{15}$$

where

$$\Delta\alpha^{(1)}_{j+\frac{1}{2},k}=\left|\frac{b^{\mathrm{W}}_{j+1,k}+b^{\mathrm{E}}_{j,k}}{2}\left(\left(h^{\mathrm{W}}_{j+1,k}+Z_{j+\frac{1}{2},k}\right)^2-\left(h^{\mathrm{E}}_{j,k}+Z_{j+\frac{1}{2},k}\right)^2\right)+h^{\mathrm{W}}_{j+1,k}(u^{\mathrm{W}}_{j+1,k})^2-h^{\mathrm{E}}_{j,k}(u^{\mathrm{E}}_{j,k})^2\right|, \tag{16a}$$

$$\Delta\alpha^{(2)}_{j+\frac{1}{2},k}=\left|h^{\mathrm{W}}_{j+1,k}(v^{\mathrm{W}}_{j+1,k})^2-h^{\mathrm{E}}_{j,k}(v^{\mathrm{E}}_{j,k})^2\right|, \tag{16b}$$

$$\Delta\alpha_{j+\frac{1}{2},k}=\sqrt{\left(\Delta\alpha^{(1)}_{j+\frac{1}{2},k}\right)^2+\left(\Delta\alpha^{(2)}_{j+\frac{1}{2},k}\right)^2}, \tag{16c}$$

and

$$\alpha_{j,k+\frac{1}{2}}=\begin{cases}\Delta\alpha^{(1)}_{j,k+\frac{1}{2}}\Big/\Delta\alpha_{j,k+\frac{1}{2}}, & \text{if } \Delta\alpha_{j,k+\frac{1}{2}}>\nu,\\ 0, & \text{otherwise,}\end{cases} \tag{17}$$

where

$$\Delta\alpha^{(1)}_{j,k+\frac{1}{2}}=\left|\frac{b^{\mathrm{S}}_{j,k+1}+b^{\mathrm{N}}_{j,k}}{2}\left(\left(h^{\mathrm{S}}_{j,k+1}+Z_{j,k+\frac{1}{2}}\right)^2-\left(h^{\mathrm{N}}_{j,k}+Z_{j,k+\frac{1}{2}}\right)^2\right)+h^{\mathrm{S}}_{j,k+1}(v^{\mathrm{S}}_{j,k+1})^2-h^{\mathrm{N}}_{j,k}(v^{\mathrm{N}}_{j,k})^2\right|, \tag{18a}$$

$$\Delta\alpha^{(2)}_{j,k+\frac{1}{2}}=\left|h^{\mathrm{S}}_{j,k+1}(u^{\mathrm{S}}_{j,k+1})^2-h^{\mathrm{N}}_{j,k}(u^{\mathrm{N}}_{j,k})^2\right|, \tag{18b}$$

$$\Delta\alpha_{j,k+\frac{1}{2}}=\sqrt{\left(\Delta\alpha^{(1)}_{j,k+\frac{1}{2}}\right)^2+\left(\Delta\alpha^{(2)}_{j,k+\frac{1}{2}}\right)^2}. \tag{18c}$$

In (15) and (17), ν is a small positive parameter designed to prevent the division by zero.

Remark 3.1: We note that using the switch parameters $\alpha_{j+\frac{1}{2},k}$ and $\alpha_{j,k+\frac{1}{2}}$ in (14) helps to reduce the amount of numerical dissipation present in central-upwind schemes without risking oscillations, as these parameters become small only near the areas of linear contact waves or shears, where much smaller amount of numerical dissipation typically suffices to stabilise the numerical solution (see Kurganov *et al.* 2019).

Equipped with the reconstructed point values and the one-sided local speeds of propagation, the central-upwind numerical fluxes can be computed using the explicit formulae provided in Appendix 2.

Remark 3.2: The resulting system of ODEs (13) should be integrated in time using a stable and sufficiently accurate ODE solver. In our simulations, we have used the three-stage third-order strong stability preserving (SSP) Runge-Kutta method (see, e.g. Gottlieb

et al. 2011, 2001) with the time steps restricted using the following CFL condition with the CFL number 1/2:

$$\Delta t = \frac{1}{2}\min\left\{\frac{\Delta x}{a^x_{\max}}, \frac{\Delta y}{a^y_{\max}}\right\},$$

where

$$a^x_{\max} := \max_{j,k}\left\{\hat{a}^+_{j+\frac{1}{2},k}, -\hat{a}^-_{j+\frac{1}{2},k}\right\}, \quad a^y_{\max} := \max_{j,k}\left\{\hat{a}^+_{j,k+\frac{1}{2}}, -\hat{a}^-_{j,k+\frac{1}{2}}\right\}. \tag{19}$$

In order to minimise the risk of instability, we use $\hat{a}^\pm_{j+\frac{1}{2},k}$ and $\hat{a}^\pm_{j,k+\frac{1}{2}}$ in (19), which are obtained using (14) with $\alpha_{j+\frac{1}{2},k} = 1$ and $\alpha_{j,k+\frac{1}{2}} = 1$.

In sections 4 and 5, we will focus on the applications of the proposed 2D well-balanced central-upwind scheme. If no otherwise specified, in all of the experiments, we assume that the bottom topography $Z(x, y) \equiv 0$, take $f_0 = 1$, $H_0 = 1$, and the switch threshold parameter $\nu = 10^{-12}$ (our numerical experiments not reported here for the sake of brevity, clearly indicate that the proposed scheme is not sensitive to the choice of ν).

4. Application 1: isolated vortices in the mid-latitude β-plane in TRSW compared to RSW

4.1. Vortex profiles and parameters

For the sake of benchmarking and continuity with the previous study (Gouzien *et al.* 2017), we consider the same family of exact solutions of (8), which are based on the non-dimensional velocity profile of the form:

$$\widetilde{V}(r) = \pm r\exp\big(-(r^\gamma - 1)/\gamma\big), \tag{20}$$

where we have used the quasi-geostrophic scaling (6) (as in Gouzien *et al.* 2017), and the positive (negative) sign correspond to cyclonic (anticyclonic) rotation in the Northern hemisphere. We take the parameter γ, which controls the steepness of the velocity profile to be equal to 3. The vorticity of such profile is $\zeta(r) = \widetilde{V}'(r) + \widetilde{V}(r)/r$, and the total vorticity $\iint_{\mathbb{R}^2}\zeta\,\mathrm{d}x\,\mathrm{d}y = 0$, which ensures that the vortex has zero circulation in the far field and thus finite total energy, that is, the vortex is *isolated*.

The corresponding profiles of non-dimensional buoyancy and thickness deviations, which satisfy the thermo-cyclogeostrophic equilibrium (8), are

$$\theta(r) = (\lambda - 1)\int_r^\infty\left(1 + Ro\,\frac{\widetilde{V}(r')}{r'}\right)\widetilde{V}(r')\,\mathrm{d}r', \tag{21}$$

where λ is a parameter, and

$$\eta(r) = \frac{\lambda}{1-\lambda}\frac{Bu}{Ro}\left(1 - 1\Big/\sqrt{1 + 2\frac{Ro}{Bu}\theta(r)}\right). \tag{22}$$

With the help of the quasi-geostrophic scaling (6), we obtain the corresponding solutions satisfying the thermo-cyclogeostrophic equilibrium (5) to be used in numerical

simulations

$$b(r) = B_0\left(1 + 2\frac{Ro}{Bu}\theta(r)\right), \quad V(r) = U\tilde{V}(r), \tag{23}$$

$$h(r) = H_0\left[1 + \frac{\lambda}{1-\lambda}\left(1 - 1\Big/\sqrt{1 + 2\frac{Ro}{Bu}\theta(r)}\right)\right]. \tag{24}$$

When $\lambda = 1$, the buoyancy is flat: $b(r) \equiv B_0$, while the thickness is recovered by substituting (21) into (24) and taking the limit as $\lambda \to 1$, which results in

$$h(r) = H_0\left[1 - \frac{Ro}{Bu}\int_r^\infty \left(1 + Ro\frac{\widetilde{V}(r')}{r'}\right)\widetilde{V}(r')\,\mathrm{d}r'\right].$$

For cyclonic vortices with positive V, which we will concentrate on in what follows, this gives a dip in h. Decreasing λ from 1 to 0 results in an admixture of a dip in buoyancy to a dip in pressure with parallel gradients of the two fields, that is, a cold-core cyclone in the oceanic, and the warm-core cyclone in the atmospheric context, as explained in section 2. At $\lambda = 0$, we have a purely "thermal" vortex with flat $h(r) \equiv H_0$. For $\lambda > 1$, we have a buoyancy bump superimposed onto the dip in pressure with antiparallel gradients of the two fields, that is, the opposite to the case $\lambda < 1$ sign of the core temperature.

4.2. Vortex instabilities: benchmark of the numerical scheme

We start with a benchmark of the developed numerical scheme, which is, in fact, a crash-test. As shown by Gouzien *et al.* (2017), the vortices with the velocity profiles (23), (20) are subject to specific small-scale instabilities of convective type. The ability of the scheme to resolve these instabilities is thus critical.

We initialise the numerical simulations (as Gouzien *et al.* 2017) by taking a purely thermal vortex with $\lambda = 0$, $B_0 = 1$, $Ro = 0.1$ and $Bu = 1$, and superimposing onto it an unstable mode with the azimuthal wavenumber $n = 3$ and a small amplitude of the order of 1% of the background vortex field. The simulation was performed in the domain $[-3, 3] \times [-3, 3]$, in the units of the deformation radius, using a uniform grid with 600×600 cells and homogeneous Neumann boundary conditions.

The time evolution of the vortex produced by this simulation is presented in figure 1. Time units here and below are $1/f_0$. The obtained results confirm the results reported by Gouzien *et al.* (2017) (see their figure 2), where the same simulation was performed at a high-resolution with a pseudospectral code and added small physical (Newtonian) viscosity, and show that the complex structures developed in the buoyancy field at later times are not numerical artifacts but physical small-scale instabilities of convective type, which are sharply captured by the proposed central-upwind scheme.

4.3. Evolution of vortices on the β-plane

In this section, we are looking for further benchmarking the developed numerical scheme, and also, once this is done, for determining the differences between the TRSW and RSW models in the description of vortex motions. We choose the so-called β-drift of localised

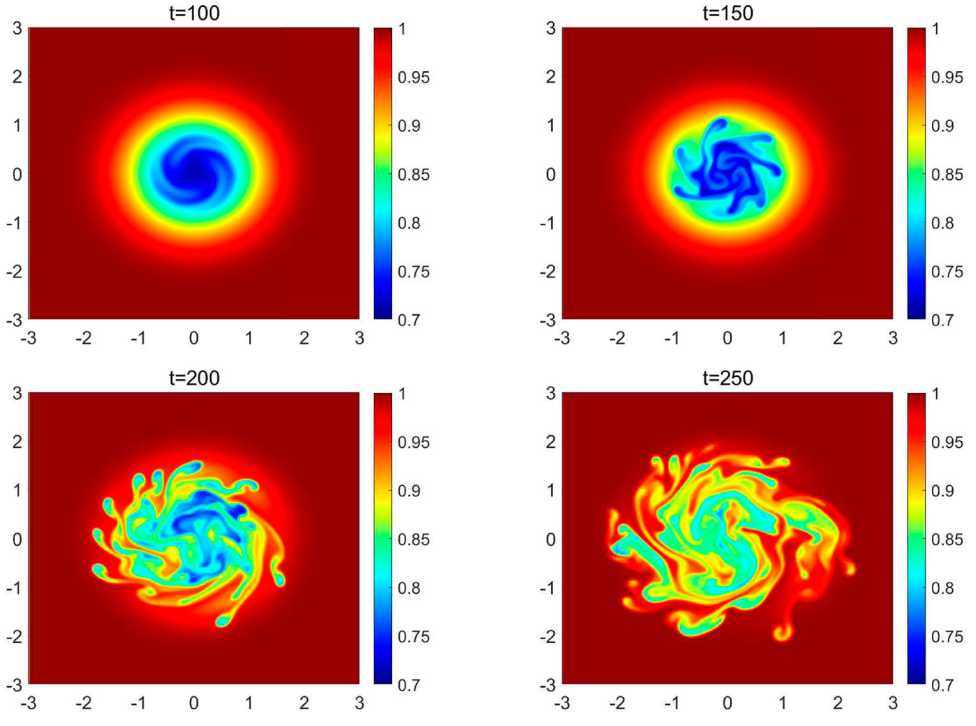

Figure 1. Snapshots of the buoyancy field during the development of the mode-3 instability of a perturbed thermal vortex; see section 4.2.

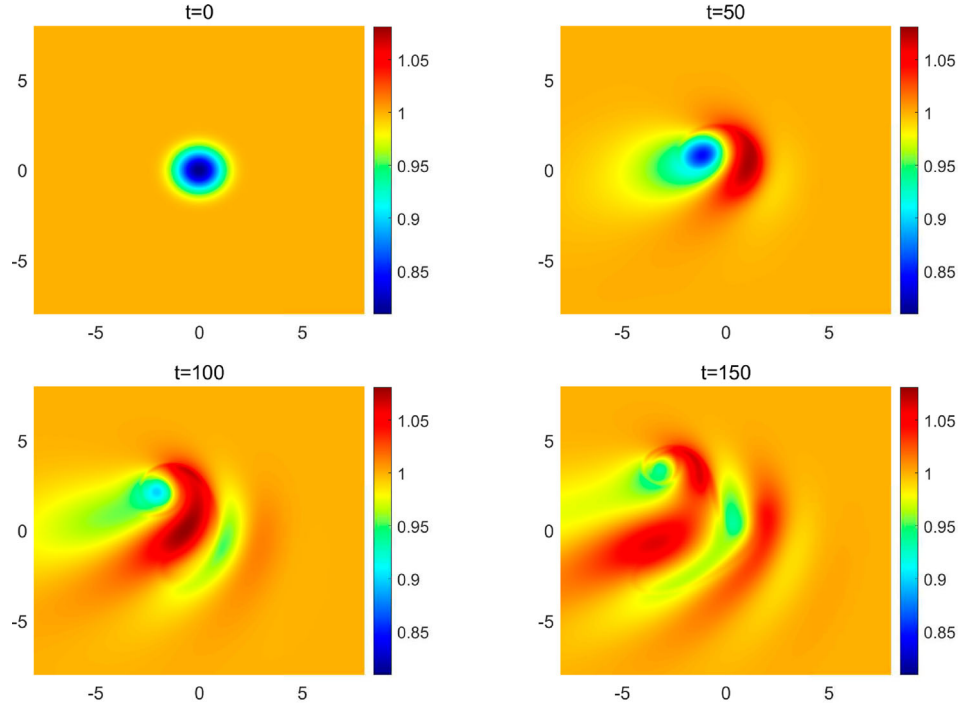

Figure 2. Same as in figure 3, but for the vortex with $\lambda = 0.8$.

vortices, which is well-known (see, e.g. Reznik and Dewar 1994, Sutyrin and Flierl 1994). It consists of the formation, due to the β-effect, of secondary vorticity structures, the β-gyres, which push the cyclonic vortex along a curved path in the North-West direction in the Northern hemisphere, that is, for positive f_0. We initialise the simulations with the vortices of the form (23), (24), which cease to be the exact solutions of the equations of motion in the presence of the β-effect. All of the simulations in this section have been performed in the domain $[-20, 20] \times [-20, 20]$, in the units of the deformation radius, using a uniform spatial grid with 1500×1500 cells and homogeneous Neumann boundary conditions. Increasing the domain size and the resolution does not sensibly affect the results. The intensity of the vortex should not be too small, as otherwise it would be rapidly dispersed as a Rossby wave-packet, and not too strong in order not to rapidly develop intrinsic instabilities, for instance, the barotropic instability expected due to a change of the vorticity gradient. This is ensured by taking the Rossby number $Ro = 0.15$. The model is considered on the β-plane with the Coriolis parameter $f(y) = 1 + 0.1y$.

We first benchmark the developed central-upwind scheme in the case of $\lambda = 1$, which corresponds to the standard RSW configuration, for which a development of β-gyres is well-documented in the literature. The evolution of thickness h and relative vorticity ζ of the cyclonic vortex are presented in figures 3 and 4, respectively. As follows from these figures, the well-known scenario of formation of secondary circulation in the form of β-gyres, a subsequent formation of the Rossby wave tail, and the curved trajectory of the core of the vortex in the North-West direction, is perfectly reproduced. The buoyancy field, which is initially flat at $\lambda = 1$ remains flat (modulo insignificant numerical noise) and is not presented.

In order to see how the temperature (buoyancy) variations across the vortex affect this scenario and, in turn, how they are influenced by it, we repeat the simulations with other values of the parameter λ, corresponding to non-flat initial b. We start with the vortex with a relatively small admixture of a dip in b to the main depression in h corresponding to $\lambda = 0.8$. The time evolution of thickness, vorticity and buoyancy in this case is presented in figures 2–6, respectively. As one can see there, the evolution of the vorticity field and the trajectory of the vortex core are practically the same as in the case of the vortex without buoyancy anomaly. The evolution of h slightly differs, which is normal, as it forms changes with adding initial b and keeping the same velocity profile. The buoyancy field itself mostly keeps coherence near the centre of the vortex, but a part of it is entrained with the Rossby wave tail.

If the buoyancy anomaly has the opposite sign, but the same amplitude (for example, if we take $\lambda = 1.2$), the evolution, which is presented for the vorticity and buoyancy fields in figures 7 and 8, respectively, is similar.

In all of the cases presented above, the vorticity evolution is practically the same and the buoyancy anomaly of relatively small amplitude mostly keeps coherence for the long time. The insight into the origins of the observed feeble difference between trajectories of thermal versus "normal" vortices in simulations presented above could be gained from the QG approximation (7) of the TRSW equations. Subtracting (7b) from (7a) we obtain

$$\left(\nabla^2\psi - \psi\right)_t + \mathcal{J}(\psi, \nabla^2\psi) = -\psi_x + \mathcal{J}(\psi, \theta). \tag{25}$$

In this form, the only difference between this equation and the standard QG equation, obtained under the same hypotheses and scaling in the RSW model, is the second term on

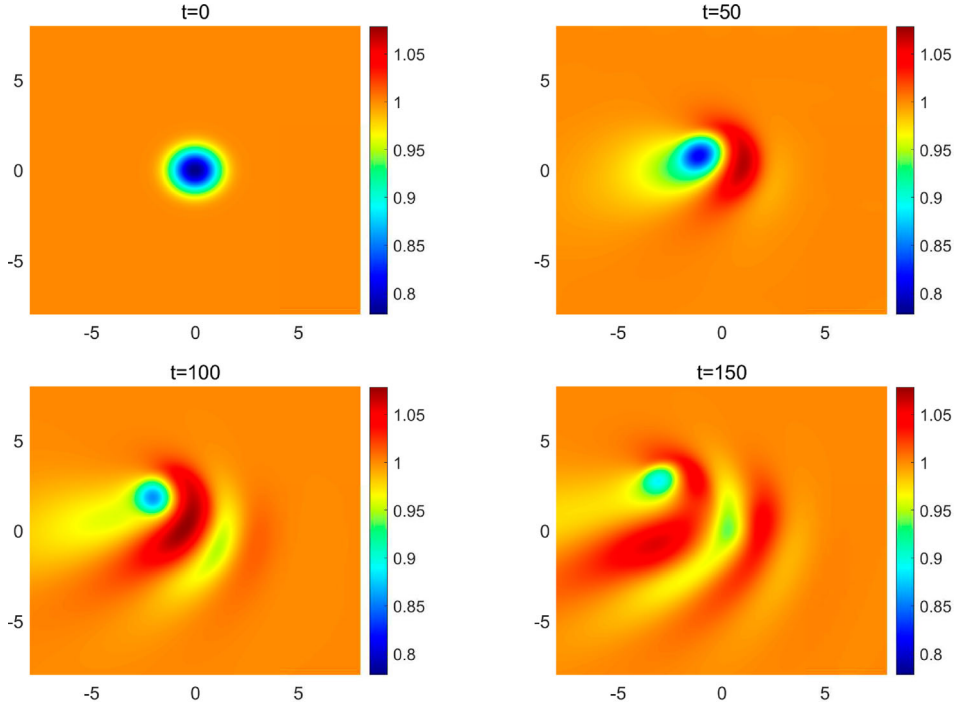

Figure 3. Snapshots of the thickness field during the time evolution of the vortex with $\lambda = 1$ on the β-plane; see section 4.3.

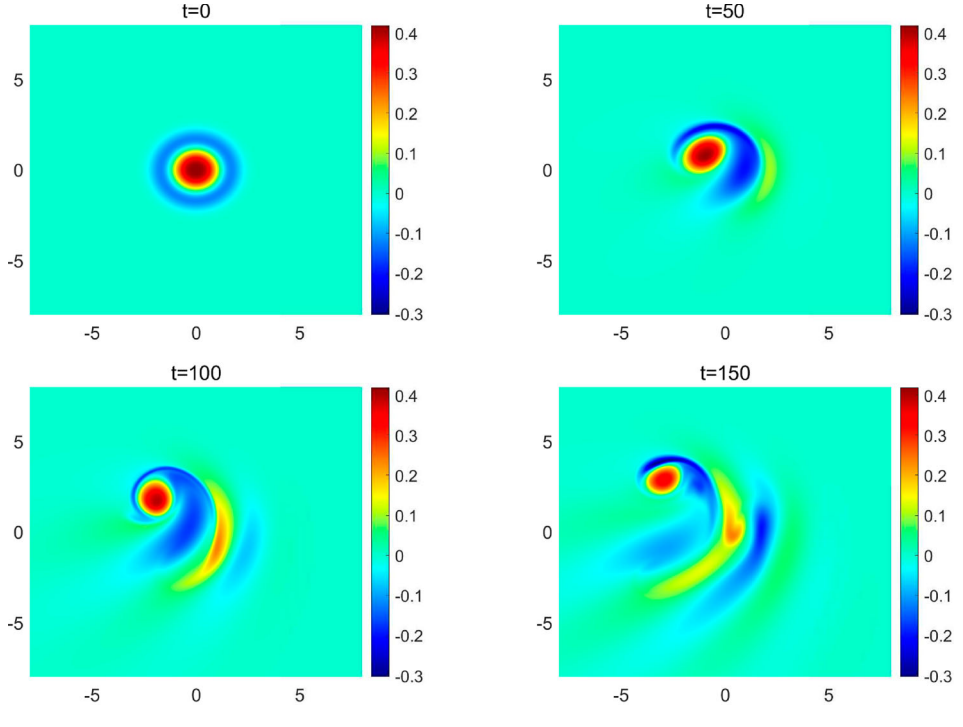

Figure 4. Same as in figure 3, but for the relative vorticity (Colour online).

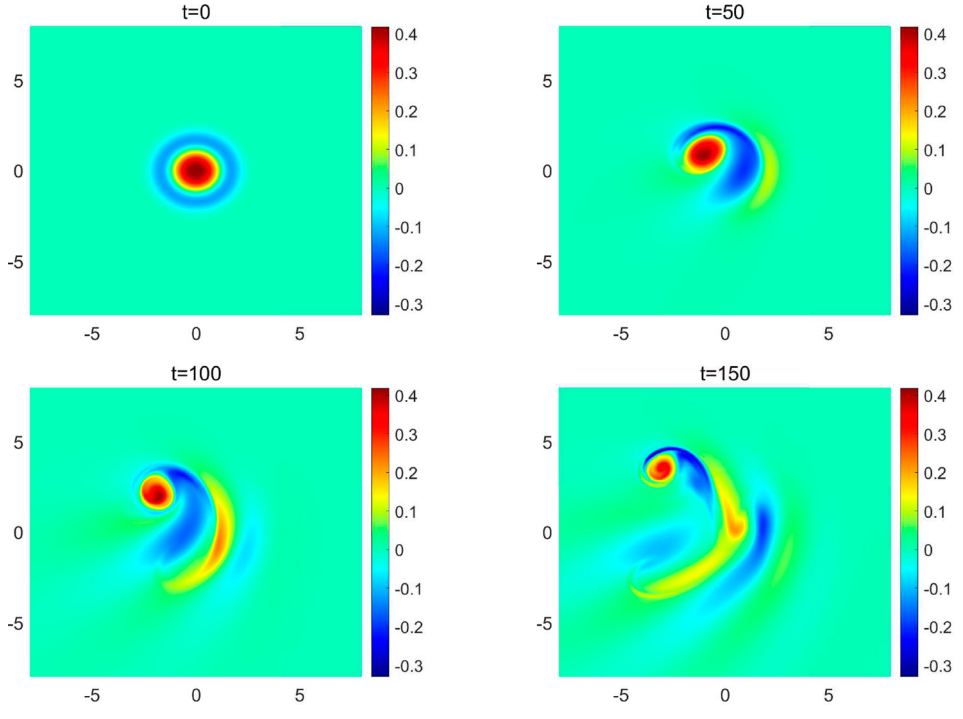

Figure 5. Same as in figure 4, but for the vortex with $\lambda = 0.8$ (Colour online).

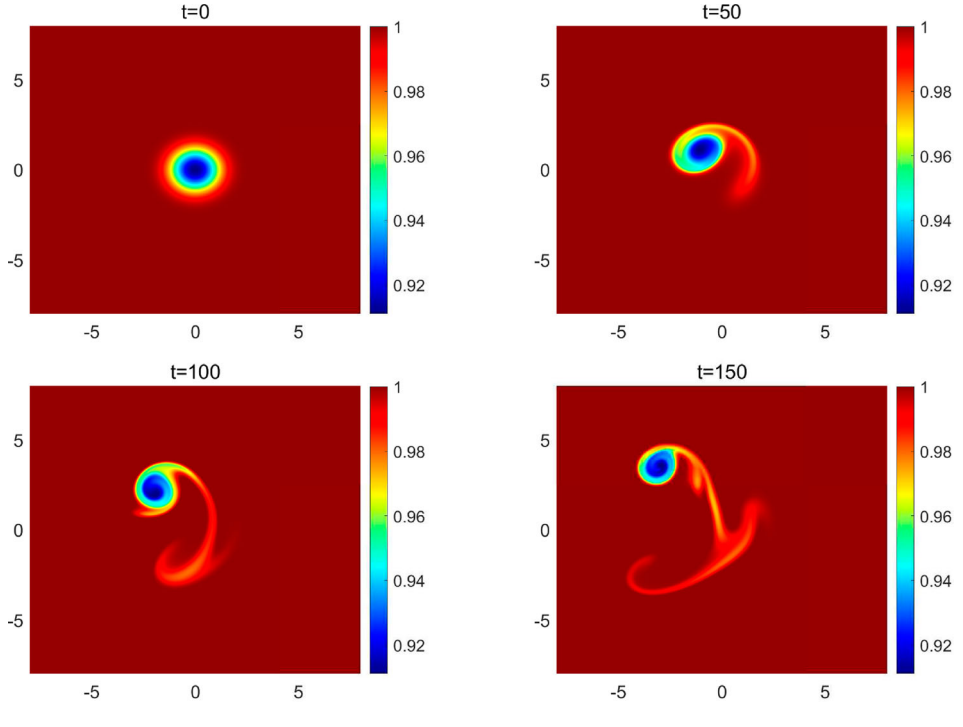

Figure 6. Same as in figures 2 and 5, but for the buoyancy field (Colour online).

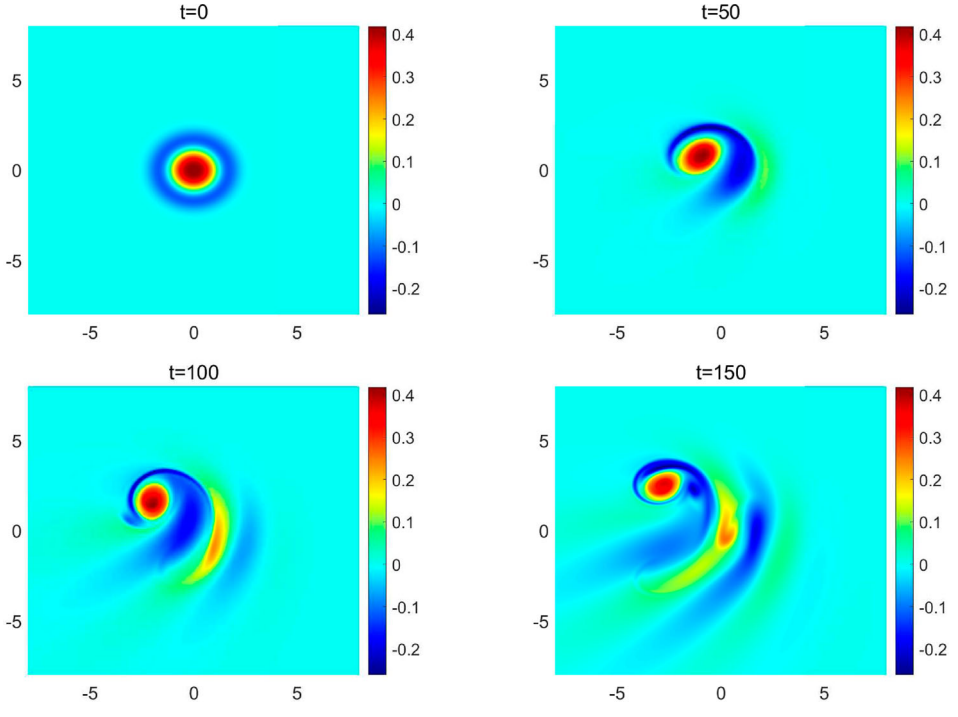

Figure 7. Same as in figure 5, but for the vortex with $\lambda = 1.2$ (Colour online).

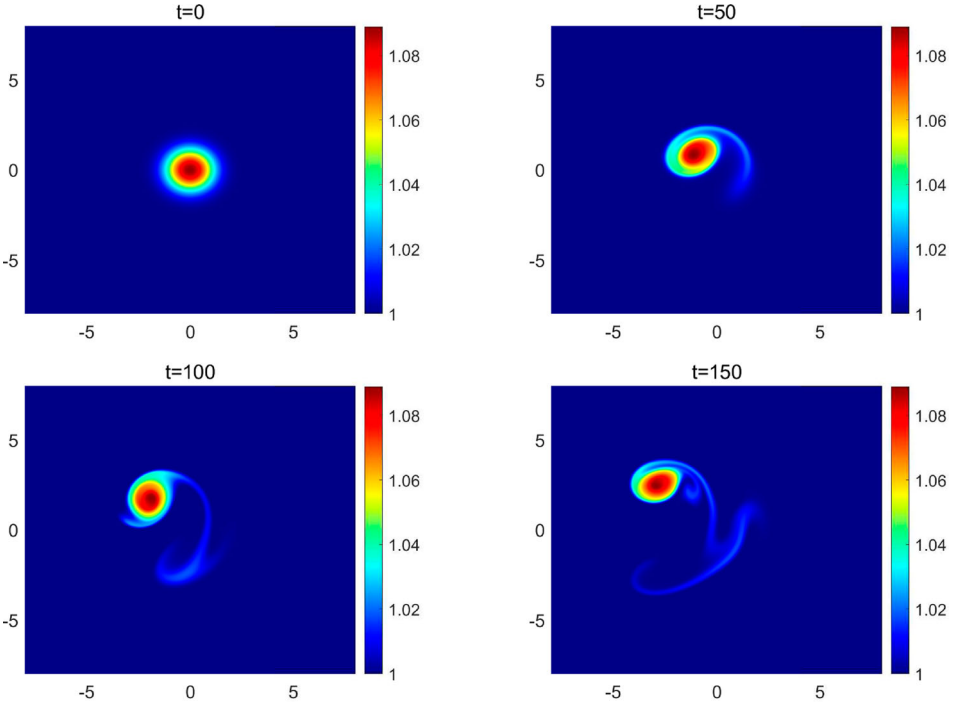

Figure 8. Same as in figure 6, but for the vortex with $\lambda = 1.2$ (Colour online).

the right-hand side, the "baroclinic" production of the geostrophic PV. Notice that the first term on the right-hand side is due to the β-effect, and is, in fact, the geostrophic meridional velocity up to a sign. Let us recall now that the standard explanation of the formation of β-gyres and of the resulting β-drift is as follows (see, e.g. Chapter 6 Zeitlin 2018). The QG PV equation is considered in the linear limit, and becomes $(\nabla^2\psi - \psi)_t = -\psi_x$, which expresses the change in the geostrophic potential vorticity and, hence, vorticity produced by the β-effect. A sign-definite localised vorticity anomaly, a vortex, is considered as an initial condition. As is easy to see, the latter leads to formation of a dipolar addition to the initial vortex, the β-gyres, as the meridional velocity of the circulation created by the vortex is opposite on the left and on the right of it. As any vortex dipole, the β-gyres tend to move along the dipole's axis, producing a displacement of the vortex as a whole; the β-drift. In turn, the primary β-gyres create further anomalies, which lead to the formation of alternating positive and negative vorticity anomalies on the right of the vortex (in the Northern hemisphere with positive f), the Rossby wave "tail". Obviously, the same analysis holds for (25), with the same conclusions, which are confirmed by the the simulations presented in this section. A difference in our case, is that the vortex is isolated, and vorticity is not sign-definite: we have a core surrounded by a ring of opposite vorticity for the profiles (20). Nevertheless, the deformation of the outer ring due to the β-effect produces the same consequences. Another reason of the small difference between the evolution of thermal and standard vortices is the conservation law (2). Indeed, as seen in figures 3–8, the contours of constant b in the vortex core change only marginally in the course of vortex evolution, which means that the absolute vorticity $\zeta + f = hQ$ inside them also changes marginally. This feeble change in the buoyancy distribution in the core region, as well as the limited influence of the baroclinic production term upon the evolution of vorticity, are also due to the initial axial symmetry and corresponding initial alignment of buoyancy and thickness perturbations, which lead to annihilation, in the leading order, of the Jacobian $\mathcal{J}(\psi, \theta)$ in (7) and (25).

However, as shown in Gouzien *et al.* (2017) and as we have seen in section 4.2, with the increase of "thermality", that is, of the strength of the buoyancy anomaly at the same velocity profile, vortices become unstable and this instability should influence their evolution. Indeed, as follows from figure 9, where we present the advanced stages of the evolution of buoyancy and vorticity in the purely thermal case ($\lambda = 0$), the vortex loses coherence and disaggregates due to the instability.

4.4. Including topography and thermal relaxation

One of important advantages of the proposed well-balanced central-upwind scheme is its ability to accurately treat the bottom topography. In order to verify this and to get insights on the interaction of vortex with the bottom topography, we repeated the experiments of section 4.3 with a non-flat bottom topography containing a ridge of Gaussian form

$$Z(x, y) = 0.1 \exp\big(-2(y - x - 8)^2\big). \tag{26}$$

The simulation is performed in the domain $[-20, 20] \times [-20, 20]$ using a uniform grid with 1500×1500 cells and the homogeneous Neumann boundary conditions.

We compare the evolution of the "normal" vortex with $\lambda = 1$ and the vortex with $\lambda = 0.8$ in the presence of the ridge. Until the time $t \approx 150$, when the vortices are sufficiently

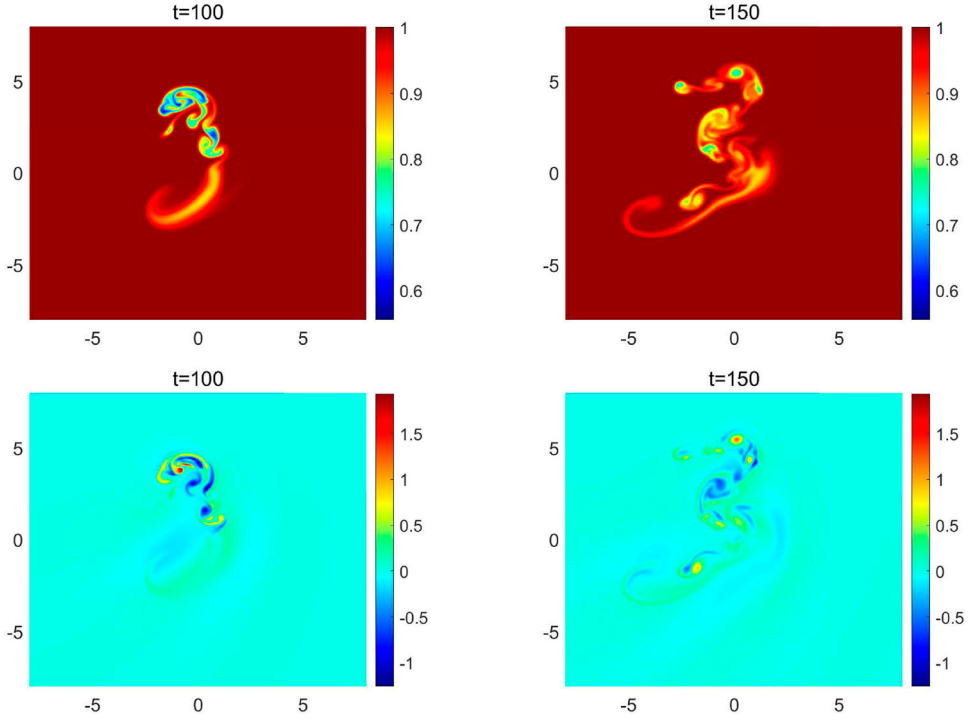

Figure 9. Snapshots of the buoyancy (upper row) and vorticity (lower row) during the time evolution of purely thermal vortex with $\lambda = 0$; see section 4.3 (Colour online).

far from the ridge, the behaviour of the vortices is the same as without ridge, which is not surprising as the ridge is upwind. Snapshots of the buoyancy and vorticity of the vortex with $\lambda = 0.8$ at later times are shown in figure 10. The vorticity of the "normal" vortex with $\lambda = 1$ at the same times is similar (not shown). As seen in figure 10, the vortex centre crosses the ridge, but undergoes a substantial stretching along the ridge, and erosion, with similar stretching and erosion of the buoyancy anomaly. This experiment demonstrates that the proposed numerical scheme is capable of tracking the fine details in the evolution of both fields.

Again, one could be surprised by a globally similar evolution of vorticity in the TRSW and RSW models, especially if one recalls that the evolution of vortices in the presence of topography is governed in the RSW model by the conservation of PV, which is not ensured in the TRSW model. However, the global PV conservation (2) is, apparently, sufficient to constrain the evolution of the TRSW case, and make it similar to that in the RSW one. It should not be forgotten that, at the same time, the TRSW model allows one to follow in a self-consistent way a simultaneous evolution of both vorticity and buoyancy anomaly, and their interactions, which is not possible in the isothermal RSW model.

We also test how the relaxation of the buoyancy field towards the mean value B_0 changes the evolution of the vortex. We included the relaxation term $-(b - B_0)/\tau$ on the right-hand side of the evolution equation for b. We take the relaxation parameter $\tau = 10$ and perform the same simulations as in section 4.3 with the $\lambda = 0.8$ vortex. We observe that while the buoyancy becomes virtually flat at $t \approx 150$, the vorticity distribution remains

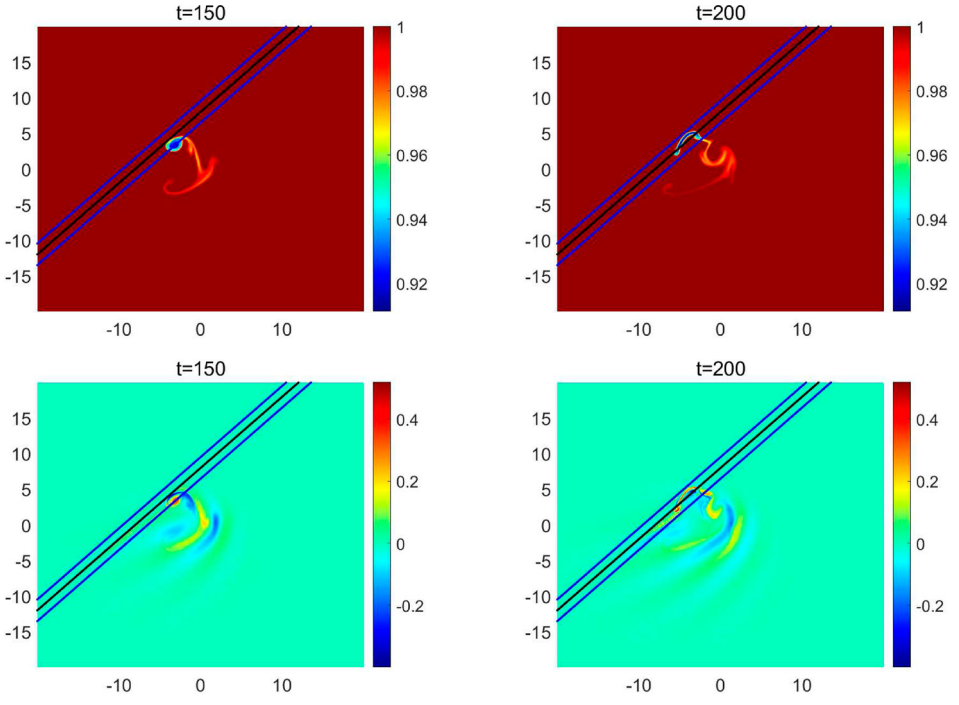

Figure 10. Snapshots of the buoyancy (upper row) and vorticity (lower row) during the time evolution of a vortex with $\lambda = 0.8$ approaching a ridge (26); see section 4.4. Position of the maximum and width of the ridge are marked by straight lines (Colour online).

practically the same as in the absence of relaxation, and the peak vorticity in the core changes little: it is 0.3495 without the relaxation of b and 0.3192 with the relaxation at $t = 150$. At the same time, the thickness anomaly deepens in the vortex core, in order to compensate for the loss of b and maintain the balance. The maximum value of the depression at $t = 150$ is 0.5694 in the absence, and 0.5579 in the presence of the relaxation of b. Therefore, we conclude that the thickness is "slaved" to vorticity, apparently because of the conservation law (2) and not the inverse, unlike the regimes close to a geostrophic balance in the RSW model (see Warn *et al.* 1995), where the velocity field and, hence, vorticity adjust to the thickness variations.

5. Application 2: relaxation of localised anomalies on the equatorial β-plane in TRSW compared to RSW

In this section, for the same purposes of benchmarking the developed central-upwind scheme and gaining insights into the differences between the TRSW and RSW models, we consider a different fundamental process: relaxation of localised perturbations on the equatorial β-plane. In order to emphasise the importance of this phenomenon, let us recall that our understanding of the circulation patterns in the tropical atmosphere is largely based on the classical paper of Gill (1980), where the RSW model on the equatorial β-plane was used to study the effects of large-scale heating by adding a source to the mass conservation equation (1b). Although it was a forced-dissipative (with an added bottom drag of the form

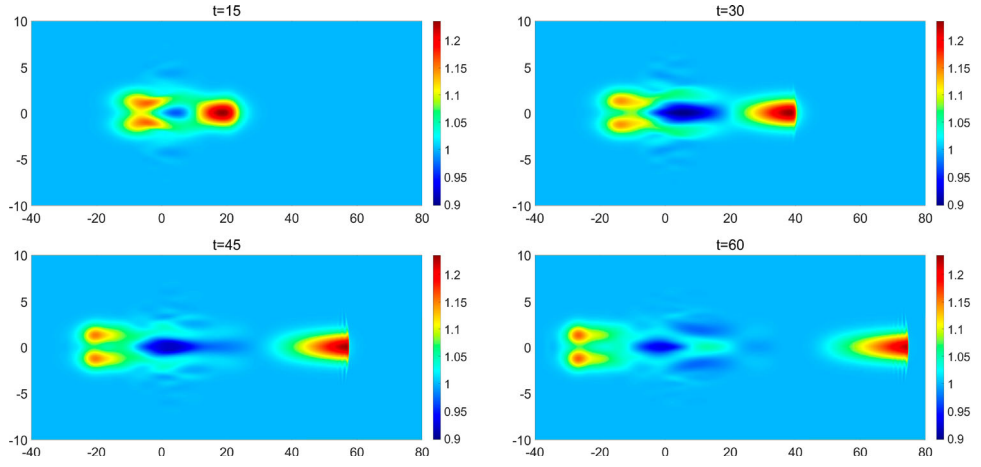

Figure 11. Snapshots of the thickness h during the time evolution of the thickness anomaly without buoyancy anomaly; see section 5 (Colour online).

discussed in section 2.2) problem which was solved in Gill (1980), the results can be understood by considering an initial value problem with a localised initial perturbation of h; the equatorial adjustment problem. In the long-wave limit used by Gill (1980), that is, for the perturbations with a small meridional to zonal aspect ratio, it was solved analytically, and the results were confirmed numerically in Le Sommer *et al.* (2004). Therefore, in order to benchmark the developed central-upwind scheme on the equatorial β-plane, we simulated the equatorial adjustment of a thickness anomaly with the following initial data

$$h(x,y,0) = 1 + 0.5\exp\left(-\frac{1}{2}\left((x/a)^2 + y^2\right)\right),$$
$$u(x,y,0) \equiv v(x,y,0) \equiv 0, \quad b(x,y,0) \equiv 1,$$

where a is the aspect ratio, which we first take to be $a = 5$. The simulation is performed in the domain $[-40, 80] \times [-10, 10]$ using a uniform grid with 1200×200 cells and the homogeneous Neumann boundary conditions. Notice that the intrinsic scale in this case is the equatorial deformation radius R_e (see below) and the natural time unit is $1/\beta R_e$, while $f_0 \equiv 0$.

The results, presented in figure 11, are fully consistent with both the theoretical analysis and numerical simulations for the RSW model on the equatorial β-plane reported by Le Sommer *et al.* (2004). One can see the formation of a Kelvin wave running eastward and steepening, because it has no dispersion, as well as the formation of a Rossby wave packet running westward, and a packet of almost standing inertia-gravity waves at the location of the initial perturbation. By itself, resolving a sharpening in time Kelvin front, which is formed by the breaking Kelvin wave, as predicted by Le Sommer *et al.* (2004) and visible in the figure 11, is a good test for a numerical method, which the developed central-upwind scheme has, thus, passed well.

Next, in order to study the difference between the adjustment of thickness and buoyancy anomalies, we initialise the simulation with the initial data corresponding to a buoyancy

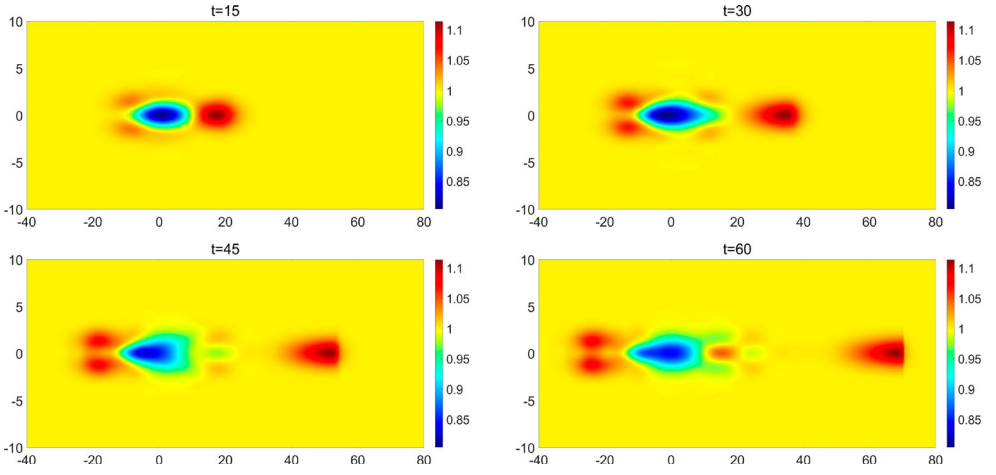

Figure 12. Snapshots of the thickness h during the time evolution of the buoyancy anomaly without thickness anomaly; see section 5 (Colour online).

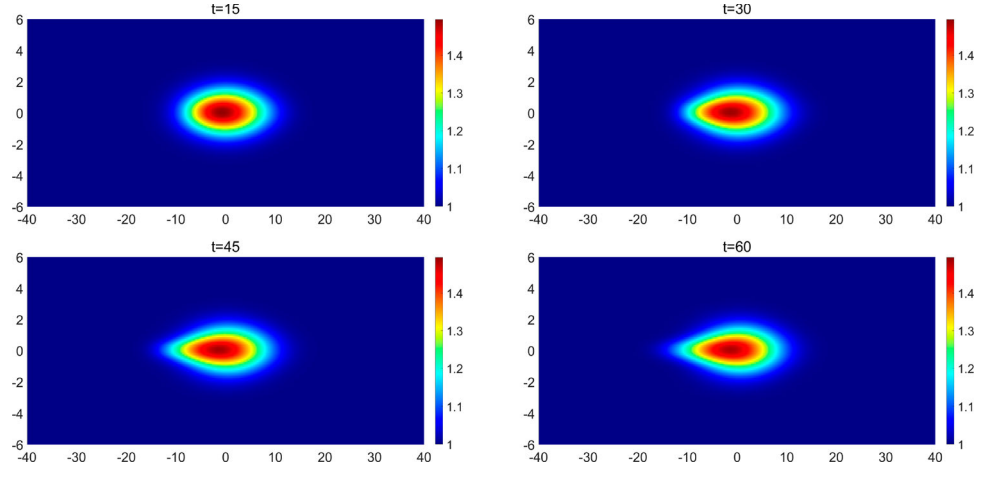

Figure 13. Snapshots of the buoyancy b during the time evolution of the buoyancy anomaly without thickness anomaly; see section 5 (Colour online).

anomaly

$$h(x,y,0) \equiv 1, \quad u(x,y,0) \equiv v(x,y,0) \equiv 0, \tag{27a,b}$$

$$b(x,y,0) = 1 + 0.5 \exp\left[-\tfrac{1}{2}\left((x/a)^2 + y^2\right)\right] \tag{27c}$$

with the aspect ratio $a = 5$. The computed thickness, presented in figure 12, shows significant differences with the previous case: although Kelvin and Rossby wave packets are also produced, their amplitudes are smaller and a quasi-stationary thickness anomaly of the opposite size arises at the location of the initial perturbation. At the same time, the buoyancy field is quasi-stationary with only marginal changes, as can be seen in figure 13.

In order to understand the differences between equatorial adjustment of the initial anomalies with flat and non-flat b, let us analyse equations (1 a–c) on the equatorial β-plane with $f(y) = \beta y$ in the long-wave approximation following the lines of Le Sommer *et al.* (2004) (see also chapter 5 Zeitlin 2018). By introducing the ratio of typical meridional to typical zonal scales $L_y/L_x := \delta \ll 1$, which is, at the same time, a ratio of the meridional to zonal velocities, supposing that the meridional scale is of the order of the equatorial deformation radius $R_e = ((B_0H_0)/\beta^2)^{1/4}$, introducing the equatorial Rossby number $\varepsilon = U/(\beta R_e^2)$, where U is the zonal velocity scale, and assuming that the motion is slow with the typical time scale $T \sim 1/(\delta\beta R_e)$, and that typical anomalies of h and b are of the order ε, we obtain the following system of non-dimensional equations for slow motions

$$u_t + \varepsilon(uu_x + vu_y) - yv = -h_x(1 + \varepsilon b) - \tfrac{1}{2}b_x(1 + \varepsilon h), \tag{28a}$$

$$\delta^2 v_t + \delta^2\varepsilon(uv_x + vv_y) + yu = -h_y(1 + \varepsilon b) - \tfrac{1}{2}b_y(1 + \varepsilon h), \tag{28b}$$

$$h_t + u_x + v_y + \varepsilon\big[(hv)_y + (hu)_x\big] = 0, \tag{28c}$$

$$b_t + \varepsilon(ub_x + vb_y) = 0. \tag{28d}$$

Following Le Sommer *et al.* (2004), this system can be studied analytically, but we will not undertake such analysis here, limiting ourselves only by considering a linear approximation of (28), which is obtained by taking the limit $\varepsilon \to 0$ and assuming that $\delta \ll \varepsilon$, which results in

$$u_t - yv = -h_x - \tfrac{1}{2}b_x, \tag{29a}$$

$$yu = -h_y - \tfrac{1}{2}b_y, \tag{29b}$$

$$h_t + u_x + v_y = 0, \tag{29c}$$

$$b_t = 0. \tag{29d}$$

Comparing with the analogous equations in the equatorial RSW model (section 5.5 Zeitlin 2018), we see that (29) is obtained by a change of variables $h \to h + b/2$ in this latter, with time-independent $b(x, y)$. This means that the standard solutions for Kelvin and long Rossby waves acquire a stationary addition in the way that only a part $\widetilde{h}(x, y, t)$ of the initial condition for the thickness field h is projected on the variable, propagative signal, while there is always a stationary part $\overline{h}\ (x, y)$. As is easy to check for the Kelvin-wave solutions with $v \equiv 0$, this stationary part should obey the equation $\overline{h}_x + b_x/2 = 0$. As follows from figures 12 and 13 (compare with figure 11), correlated stationary signals in h and b do appear in the TRSW model. Moreover, at the same amplitude but with even larger aspect ratio $a = 10$ in (27), the buoyancy field in analogous simulation practically does not change at all (not shown). An important conclusion that can drawn from these simulations and analysis is that stronger non-linearities and aspect ratios of order 1 are needed to make the initial buoyancy significantly evolve, otherwise it serves only as a catalyzer for triggering the evolution of pressure.

Let us also emphasise that an important feature of curved shocks in shallow water models in general, and in particular on the equatorial β-plane (see Bouchut *et al.* 2005), is generation of vorticity and potential vorticity behind them. An analysis of the Rankine–Hugoniot conditions (9), which can be performed following the lines of Le Sommer

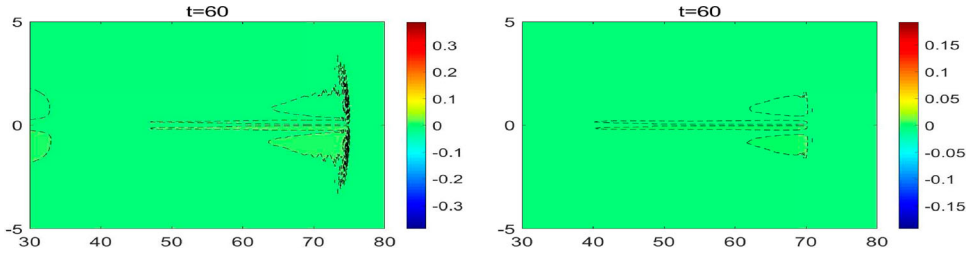

Figure 14. Snapshots of the PV anomaly behind the Kelvin fronts on the lower-right panels of figures 11 (left) and 12 (right) (Colour online).

et al. (2004) (see also references therein), shows that a dipolar anomaly of potential vorticity should appear behind the Kelvin front. Reproducing this phenomenon is one of the tests for the proposed TRSW model and central-upwind scheme. In figure 14, we present the potential vorticity anomaly associated to the Kelvin front, which is clearly visible in the lower-right panels of figures 11 and 12, respectively, and showing that the front indeed generates a potential vorticity dipole, which is weaker in the simulation of figure 12 because of a weaker intensity of the thickness perturbation.

6. Summary and conclusions

We have constructed and presented in a ready-to-code form a well-balanced high-resolution numerical scheme for the TRSW model and tested it on two classical geophysical fluid dynamics processes: evolution of localised vortices on the β-plane, including their interaction with an idealised mountain ridge, and relaxation of localised pressure and temperature anomalies at the equator. Our main goal was not an in-depth investigation in either case, but a demonstration of capabilities of the new scheme. Nevertheless, we have obtained some new and somewhat unexpected results. A disadvantage of the TRSW model, which sometimes is presented as a handicap, is the absence of Lagrangian conservation of the PV. An important conclusion of the present work is that the absence of Lagrangian PV conservation in the model has no drastic consequences. We have observed no dramatic changes in the evolution of vorticity of convectively-stable thermal vortices on the β-plane and their interactions with topography, compared to the standard RSW results. Part of the explanation of this fact is given by the initial alignment of buoyancy and thickness in the vortices, but the global conservation of PV matters too, although its precise role in the presence of topography requires further investigation. The observed slaving of pressure to vorticity is also worth noting. Overall, we have shown that our scheme is capable of high-resolution tracking of both the vorticity and active scalar during the motion of isolated oceanic vortices and their interaction with bathymetry. In spite of the fact that in the examples we have presented, the evolution of vorticity is close to what is expected in the isothermal RSW model, it should be not forgotten that the TRSW model allows one to simulate configurations which can not be captured by the RSW equations in a self-consistent way, like interaction of vortices with variable-temperature (or salinity) background, preserving, at the same time, the simplicity of shallow water modelling.

Another important conclusion is that in the long-wave approximation, which is traditionally used in the analysis of tropical circulation starting from the pioneering work

(Gill 1980), the buoyancy, that is, the potential temperature in the atmospheric context, acts mainly as a catalyzer of pressure evolution not much changing itself in the absence of diabatic effects in the TRSW model.

An advantage of the studied model, and its *raison d'être* is its ability to represent simultaneously sharp pressure and temperature fronts. The presented numerical scheme is able to properly resolve them (shock-capturing property), as we shown on the example of equatorial Kelvin fronts, and, at the same time, to maintain the equilibrium states at the discrete level (well-balanced property), as well as to capture small-scale convective-type instabilities which are proper to the TRSW model.

Acknowledgements

The work of A. Kurganov was supported in part by NSFC grant 11771201 and by the fund of the Guangdong Provincial Key Laboratory of Computational Science and Material Design (No. 2019B030301001). The work of A. Kurganov and V. Zeitlin was supported in part by the French National Program LEFE-MANU.

Disclosure statement

No potential conflict of interest was reported by the author(s).

Funding

The work of A. Kurganov was supported in part by NSFC grant 11771201 and by the fund of the Guangdong Provincial Key Laboratory of Computational Science and Material Design (No. 2019B030301001). The work of A. Kurganov and V. Zeitlin was supported in part by the French National Program LEFE-MANU. Centre National de la Recherche Scientifique

ORCID

Yongle Liu http://orcid.org/0000-0002-6197-957X

References

Bollermann, A., Noelle, S. and Lukáčová-Medviďová, M., Finite volume evolution Galerkin methods for the shallow water equations with dry beds. *Commun. Comput. Phys.* 2011, **10**, 371–404.

Bouchut, F., Le Sommer, J. and Zeitlin, V., Breaking of balanced and unbalanced equatorial waves. *Chaos* 2005, **15**, 013503.

Cheng, Y., Chertock, A., Herty, M., Kurganov, A. and Wu, T., A new approach for designing moving-water equilibria preserving schemes for the shallow water equations. *J. Sci. Comput.* 2019, **80**, 538–554.

Cheng, Y. and Kurganov, A., Moving-water equilibria preserving central-upwind schemes for the shallow water equations. *Commun. Math. Sci.* 2016, **14**, 1643–1663.

Chertock, A., Cui, S., Kurganov, A., Özcan, Ş.N. and Tadmor, E., Well-balanced schemes for the Euler equations with gravitation: Conservative formulation using global fluxes. *J. Comput. Phys.* 2018a, **358**, 36–52.

Chertock, A., Dudzinski, M., Kurganov, A. and Lukáčová-Medviďová, M., Well-balanced schemes for the shallow water equations with Coriolis forces. *Numer. Math.* 2018b, **138**, 939–973.

Chertock, A., Herty, M. and Özcan, Ş.N., Well-balanced central-upwind schemes for 2×2 systems of balance laws. In *Theory, Numerics and Applications of Hyperbolic Problems. I*, Springer Proc. Math. Stat., edited by C. Klingenberg and M. Westdickenberg, Vol. 236 of *Springer Proc. Math. Stat.*, pp. 345–361, 2018c (Springer: Cham).

Chertock, A., Kurganov, A. and Liu, Y., Central-upwind schemes for the system of shallow water equations with horizontal temperature gradients. *Numer. Math.* 2014, **127**, 595–639.
Cho, J.Y.K., Menou, K., Hansen, B. M. S. and Seager, S., Atmospheric circulation of close-in extrasolar giant planets. I. Global, barotropic, adiabatic simulations. *Astroph. J.* 2008, **675**, 817–845.
Dempsey, D.P. and Rotunno, R., Topographic generation of mesoscale vortices in mixed-layer models. *J. Atmos. Sci.* 1988, **45**, 2961–2978.
Gill, A., Some simple solutions for heat induced tropical circulation. *Q. J. Roy. Met. Soc.* 1980, **106**, 447–462.
Gottlieb, S., Ketcheson, D. and Shu, C.W., *Strong Stability Preserving Runge-Kutta and Multistep Time Discretizations*, 2011 (World Scientific Publishing Co. Pte. Ltd.: Hackensack, NJ).
Gottlieb, S., Shu, C.W. and Tadmor, E., Strong stability-preserving high-order time discretization methods. *SIAM Rev.* 2001, **43**, 89–112.
Gouzien, E., Lahaye, N., Zeitlin, V. and Dubos, T., Thermal instability in rotating shallow water with horizontal temperature/density gradients. *Phys. Fluids* 2017, **29**, 101702.
Halverson, J.B., Simpson, J., Heymsfield, G., Pierce, H., Hock, T. and Ritchie, L., Warm-core structure of Hurricane Erin diagnosed from high-altitude dropsondes during CAMEX-4. *J. Atmos. Sci.* 2006, **63**, 309–324.
Kurganov, A., Central schemes: A powerful black-box solver for nonlinear hyperbolic PDEs. In *Handbook of Numerical Methods for Hyperbolic Problems*, Handb. Numer. Anal., edited by R. Abgrall and C.W. Shu, Vol. 17 of *Handb. Numer. Anal.*, pp. 525–548, 2016 (Elsevier/North-Holland: Amsterdam).
Kurganov, A., Finite-volume schemes for shallow-water equations. *Acta Numer.* 2018, **27**, 289–351.
Kurganov, A. and Lin, C.T., On the reduction of numerical dissipation in central-upwind schemes. *Commun. Comput. Phys.* 2007, **2**, 141–163.
Kurganov, A., Liu, Y. and Zeitlin, V., Numerical dissipation switch for two-dimensional central-upwind schemes. *Submitted*, 2019 Preprint available at https://sites.google.com/view/alexander-kurganov/publications.
Kurganov, A., Liu, Y. and Zeitlin, V., A well-balanced central-upwind scheme for the thermal rotating shallow water equations. *J. Comput. Phys.* 2020, **411**, 109414.
Kurganov, A., Noelle, S. and Petrova, G., Semidiscrete central-upwind schemes for hyperbolic conservation laws and Hamilton-Jacobi equations. *SIAM J. Sci. Comput.* 2001, **23**, 707–740.
Kurganov, A. and Petrova, G., A second-order well-balanced positivity preserving central-upwind scheme for the Saint-Venant system. *Commun. Math. Sci.* 2007, **5**, 133–160.
Kurganov, A. and Tadmor, E., New high-resolution central schemes for nonlinear conservation laws and convection–diffusion equations. *J. Comput. Phys.* 2000, **160**, 241–282.
Kurganov, A. and Tadmor, E., Solution of two-dimensional Riemann problems for gas dynamics without Riemann problem solvers. *Numer. Methods Partial Differ. Equ.* 2002, **18**, 584–608.
Lavoie, R.L., A mesoscale numerical model of lake-effect storms. *J. Atmos. Sci.* 1972, **29**, 1025–1040.
Le Sommer, J., Reznik, G.M. and Zeitlin, V., Nonlinear geostrophic adjustment of long-wave disturbances in the shallow-water model on the equatorial beta-plane. *J. Fluid Mech.* 2004, **515**, 135–170.
Lie, K.A. and Noelle, S., On the artificial compression method for second-order nonoscillatory central difference schemes for systems of conservation laws. *SIAM J. Sci. Comput.* 2003, **24**, 1157–1174.
McCreary, J.P., Kundu, P.K. and Molinari, R.L., A numerical investigation of dynamics, thermodynamics and mixed-layer processes in the Indian Ocean. *Prog. Oceanog.* 1993, **31**, 181–244.
Nessyahu, H. and Tadmor, E., Nonoscillatory central differencing for hyperbolic conservation laws. *J. Comput. Phys.* 1990, **87**, 408–463.
Reznik, G.M. and Dewar, W., An analytical theory of distributed axisymmetric barotropic vortices on the beta-plane. *J. Fluid Mech.* 1994, **269**, 301–321.
Ripa, P., On improving a one-layer ocean model with thermodynamics. *J. Fluid Mech.* 1995, **303**, 169–201.
Salby, M.L., Deep circulations under simple classes of stratification. *Tellus* 1989, **41A**, 48–65.

Sánchez-Linares, C., Morales de Luna, T. and Castro Díaz, M.J., A HLLC scheme for Ripa model. *Appl. Math. Comput.* 2016, **272**, 369–384.
Stone, P.H., On non-geostrophic baroclinic instability. *J. Atmos. Sci.* 1966, **23**, 390–400.
Sun, W., Dong, C., Tan, W. and He, Y., Statistical characteristics of cyclonic warm-core eddies and anticyclonic cold-core eddies in the North Pacific based on remote sensing data. *Remote Sens.* 2019, **11**, 208.
Sutyrin, G.G. and Flierl, G.R., Intense vortex motionon the beta plane: Development of the beta gyres. *J. Atmos Sci.* 1994, **51**, 773–790.
Sweby, P.K., High resolution schemes using flux limiters for hyperbolic conservation laws. *SIAM J. Numer. Anal.* 1984, **21**, 995–1011.
van Leer, B., Towards the ultimate conservative difference scheme. V. A second-order sequel to Godunov's method. *J. Comput. Phys.* 1979, **32**, 101–136.
Warn, T., Bokhove, O., Shepherd, T.G. and Vallis, G.K., Rossby number expansions, slaving principles, and balanced dynamics. *Q. J. Roy. Met. Soc.* 1995, **121**, 723–739.
Warneford, E.S. and Dellar, P.J., The quasi-geostrophic theory of the thermal shallow water equations. *J. Fluid Mech.* 2013, **723**, 374–403.
Warnerford, E.S. and Dellar, P.J., Thermal shallow water models of geostrophic turbulence in Jovian atmospheres. *Phys. Fluids* 2014, **26**, 016603.
Young, W.R., The subinertial mixed layer approximation. *J. Phys. Oceanogr.* 1994, **24**, 1812–1826.
Young, W.R. and Chen, L., Baroclinic instability and thermohaline alignment in the mixed layer. *J. Phys. Oceanogr.* 1995, **25**, 3172–3185.
Zeitlin, V., *Geophysical Fluid Dynamics: Understanding (almost) Everything with Rotating Shallow Water Models*, 2018 (Oxford University Press: Oxford).
Zerroukat, M. and Allen, T., A moist Boussinesq shallow water equations set for testing atmospheric models. *J. Comp. Phys.* 2015, **290**, 55–72.

Appendices

Appendix 1. Well-balanced piecewise linear reconstruction

As in the 1D case studied by Kurganov *et al.* (2020), instead of reconstructing the conservative variables, we perform piecewise polynomial reconstruction of equilibrium variables (see also Kurganov and Petrova 2007, Cheng and Kurganov 2016, Chertock *et al.* 2018a, 2018b, 2018c, Kurganov 2018, Cheng *et al.* 2019). In order to design a second-order scheme, one needs to reconstruct a piecewise linear interpolant out of the available set of cell averages. We apply a piecewise linear reconstruction in a piecewise component manner as it is commonly done in Riemann-problem-solver-free Godunov-type schemes (see, e.g. the review papers and references therein Kurganov 2016, 2018). We first present a general piecewise linear reconstruction approach. To this end, we assume that for the reconstructed quantity φ, either the cell averages, $\{\overline{\varphi}_{j,k}\}$, or point values, $\{\varphi_{j,k}\}$, are available. We then obtain a global spatial approximant

$$\widetilde{\varphi}(x,y) = \overline{\varphi}_{j,k} + (\varphi_x)_{j,k}(x-x_j) + (\varphi_y)_{j,k}(y-y_k), \quad (x,y) \in C_{j,k}, \tag{A1}$$

where $(\varphi_x)_{j,k}$ and $(\varphi_y)_{j,k}$ are at least first-order approximations of the derivatives $\varphi_x(x_j,y_k)$ and $\varphi_y(x_j,y_k)$, respectively (if the reconstruction is build out of the point values, then the cell average $\overline{\varphi}_{j,k}$ in (A1), as well as in (A2)–(A3) below, should be replaced with the corresponding point value $\varphi_{j,k}$). It is well-known that in order to make the reconstruction (A1) non-oscillatory, the slopes are to be computed using a nonlinear limiter. We have used the generalised minmod limiter (see, e.g. van Leer 1979, Sweby 1984, Nessyahu and Tadmor 1990, Lie and Noelle 2003)

$$(\varphi_x)_{j,k} = \text{minmod}\left(\theta\frac{\overline{\varphi}_{j,k}-\overline{\varphi}_{j-1,k}}{\Delta x}, \frac{\overline{\varphi}_{j+1,k}-\overline{\varphi}_{j-1,k}}{2\Delta x}, \theta\frac{\overline{\varphi}_{j+1,k}-\overline{\varphi}_{j,k}}{\Delta x}\right), \tag{A2a}$$

$$(\varphi_y)_{j,k} = \text{minmod}\left(\theta\frac{\overline{\varphi}_{j,k}-\overline{\varphi}_{j,k-1}}{\Delta y}, \frac{\overline{\varphi}_{j,k+1}-\overline{\varphi}_{j,k-1}}{2\Delta y}, \theta\frac{\overline{\varphi}_{j,k+1}-\overline{\varphi}_{j,k}}{\Delta y}\right), \tag{A2b}$$

where the parameter $\theta \in [1,2]$ helps to control the amount of numerical diffusion (larger values of θ correspond to less diffusive, but more oscillatory reconstruction), and the minmod function is defined by

$$\text{minmod}(\omega_1,\omega_2,\ldots) := \begin{cases} \min_k\{\omega_k\}, & \text{if } \omega_k > 0 \ \forall k, \\ \max_k\{\omega_k\}, & \text{if } \omega_k < 0 \ \forall k, \\ 0, & \text{otherwise,} \end{cases}$$

and applied in (A2) in a component-wise manner.

Equipped with the reconstruction (A1), (A2), we can compute the point values of φ at the four cell interfaces $(x_{j\pm\frac{1}{2}}, y_k)$ and $(x_j, y_{k\pm\frac{1}{2}})$

$$\varphi^{\mathrm{E}}_{j,k} = \overline{\varphi}_{\,j,k} + \tfrac{1}{2}\,\Delta x\,(\varphi_x)_{j,k}, \qquad \varphi^{\mathrm{W}}_{j,k} = \overline{\varphi}_{\,j,k} - \tfrac{1}{2}\,\Delta x\,(\varphi_x)_{j,k}, \tag{A3a,b}$$

$$\varphi^{\mathrm{N}}_{j,k} = \overline{\varphi}_{\,j,k} + \tfrac{1}{2}\,\Delta y\,(\varphi_y)_{j,k}, \qquad \varphi^{\mathrm{S}}_{j,k} = \overline{\varphi}_{\,j,k} - \tfrac{1}{2}\,\Delta y\,(\varphi_y)_{j,k}. \tag{A3c,d}$$

We note that in order to compute $\varphi^{\mathrm{E}}_{j,k}$ and $\varphi^{\mathrm{W}}_{j,k}$, we only need to evaluate the x-slope, while computing $\varphi^{\mathrm{N}}_{j,k}$ and $\varphi^{\mathrm{S}}_{j,k}$ requires the y-slope only. We use this fact and reconstruct the East and West values of the variables q, p, K and b, while the North and South values are obtained for q, p, L and b since K is the second component of the x-flux, while L is the third component of the x-flux; see (11).

Before the reconstruction can be performed for the aforementioned equilibrium variables, we need to obtain the point values of b, K and L. First, we immediately obtain $b_{j,k} := \overline{(hb)}_{\,j,k} / \overline{h}_{\,j,k}$. The point values of K and L are computed as follows

$$K_{j,k} = \big(\overline{q}^{\,2}_{j,k} / \overline{h}_{\,j,k}\big) + \tfrac{1}{2}\,\overline{(hb)}_{\,j,k}\,\overline{h}_{\,j,k} + Q_{j,k}, \quad j = 1,\ldots,N_x, \quad k = 1,\ldots,N_y, \tag{A4a}$$

$$L_{j,k} = \big(\overline{p}^{\,2}_{j,k} / \overline{h}_{\,j,k}\big) + \tfrac{1}{2}\,\overline{(hb)}_{\,j,k}\,\overline{h}_{\,j,k} + R_{j,k}, \quad j = 1,\ldots,N_x, \quad k = 1,\ldots,N_y, \tag{A4b}$$

where N_x and N_y are the total number of cells in the x-and y-directions, respectively. The global parts of the flux variables, $Q_{j,k}$ and $R_{j,k}$, are defined as

$$Q_{j,k} = \int^{x_j} \Big[-f(y_k)p(\xi,y_k) + h(\xi,y_k)b(\xi,y_k)Z_x(\xi,y_k)\Big]\,\mathrm{d}\xi, \tag{A5a}$$

$$R_{j,k} = \int^{y_k} \Big[f(\xi)q(x_j,\xi) + h(x_j,\xi)b(x_j,\xi)Z_y(x_j,\xi)\Big]\,\mathrm{d}\xi. \tag{A5b}$$

We then apply the trapezoidal quadrature to discretise the integrals in (A5) and compute $Q_{j,k}$ and $R_{j,k}$ in a recursive way

$$\begin{aligned} Q_{j,k} = Q_{j-1,k} &- \tfrac{1}{2}(\Delta x)\,f_k\big(\overline{p}_{\,j-1,k} + \overline{p}_{\,j,k}\big) \\ &+ \tfrac{1}{2}\Big[\overline{(hb)}_{\,j-1,k} + \overline{(hb)}_{\,j,k}\Big]\big(Z_{j,k} - Z_{j-1,k}\big), \end{aligned} \tag{A6a}$$

$$\begin{aligned} R_{j,k} = R_{j,k-1} &+ \tfrac{1}{2}(\Delta y)\,\big(f_{k-1}\,\overline{q}_{\,j,k-1} + f_k\,\overline{q}_{\,j,k}\big) \\ &+ \tfrac{1}{2}\Big[\overline{(hb)}_{\,j,k-1} + \overline{(hb)}_{\,j,k}\Big]\big(Z_{j,k} - Z_{j,k-1}\big), \end{aligned} \tag{A6b}$$

where $f_k := f(y_k)$, $Q_{1,k} = (Q_{1/2,k} + Q_{3/2,k})/2$ and $R_{j,1} = (R_{j,1/2} + R_{j,3/2})/2$. The values of Q and R at the cell interfaces are computed using the midpoint rule as follows

$$Q_{j+\frac{1}{2},k} = Q_{j-\frac{1}{2},k} - f_k\,\overline{p}_{\,j,k}\Delta x + \overline{(hb)}_{\,j,k}\big(Z_{j+\frac{1}{2},k} - Z_{j-\frac{1}{2},k}\big), \tag{A7a}$$

$$R_{j,k+\frac{1}{2}} = R_{j,k-\frac{1}{2}} + f_k\,\overline{q}_{\,j,k}\Delta y + \overline{(hb)}_{\,j,k}\big(Z_{j,k+\frac{1}{2}} - Z_{j,k-\frac{1}{2}}\big). \tag{A7b}$$

Here, we initialise the recursive computations by setting $Q_{1/2,k} := 0,\ \forall k$ and $R_{j,1/2} := 0,\ \forall j$.

The point values of Z used in (A6) and (A7) are computed using a continuous bilinear interpolant (see Kurganov and Petrova 2007, Kurganov 2018), which gives

$$Z_{j,k}=\frac{1}{4}\left(Z_{j+\frac{1}{2},k+\frac{1}{2}}+Z_{j+\frac{1}{2},k-\frac{1}{2}}+Z_{j-\frac{1}{2},k+\frac{1}{2}}+Z_{j-\frac{1}{2},k-\frac{1}{2}}\right),$$

$$Z_{j+\frac{1}{2},k}=\frac{1}{2}\left(Z_{j+\frac{1}{2},k+\frac{1}{2}}+Z_{j+\frac{1}{2},k-\frac{1}{2}}\right),\quad Z_{j,k+\frac{1}{2}}=\frac{1}{2}\left(Z_{j+\frac{1}{2},k+\frac{1}{2}}+Z_{j-\frac{1}{2},k+\frac{1}{2}}\right).$$

Here, $Z_{j\pm1/2,k\pm1/2}$ are the point values of Z at the corners of the cell $C_{j,k}$, that is, $Z_{j\pm1/2,k\pm1/2}=Z(x_{j\pm1/2},y_{k\pm1/2})$ when the bottom topography is continuous. For the case of discontinuous Z, we refer the reader to Kurganov (2018) and Kurganov and Petrova (2007).

Finally, similarly to the 1D case studied by Kurganov *et al.* (2020), we compute the values of h at the cell interfaces by solving the following four cubic equations, which are obtained using the definitions of global variables K and L in (12),

$$(q^{\rm E}_{j,k})^2/h^{\rm E}_{j,k}+\tfrac{1}{2}b_{j+\frac{1}{2},k}(h^{\rm E}_{j,k})^2+Q_{j+\frac{1}{2},k}-K^{\rm E}_{j,k}=0, \tag{A8a}$$

$$(q^{\rm W}_{j,k})^2/h^{\rm W}_{j,k}+\tfrac{1}{2}b_{j+\frac{1}{2},k}(h^{\rm W}_{j,k})^2+Q_{j+\frac{1}{2},k}-K^{\rm W}_{j,k}=0, \tag{A8b}$$

$$(p^{\rm N}_{j,k})^2/h^{\rm N}_{j,k}+\tfrac{1}{2}b_{j,k+\frac{1}{2}}(h^{\rm N}_{j,k})^2+R_{j,k+\frac{1}{2}}-L^{\rm N}_{j,k}=0, \tag{A8c}$$

$$(p^{\rm S}_{j,k})^2/h^{\rm S}_{j,k}+\tfrac{1}{2}b_{j,k+\frac{1}{2}}(h^{\rm S}_{j,k})^2+R_{j,k+\frac{1}{2}}-L^{\rm S}_{j,k}=0, \tag{A8d}$$

where $Q_{j+\frac{1}{2},k}$ and $R_{j,k+\frac{1}{2}}$ are defined in (A7), and the corresponding point values of q, p, K and L are obtained using the piecewise linear reconstruction of these variables. Furthermore, in order to enforce a well-balanced property (see Kurganov *et al.* 2020), we set

$$b_{j+\frac{1}{2},k}:=\frac{1}{2}\left(b^{\rm E}_{j,k}+b^{\rm W}_{j+1,k}\right)\quad\text{and}\quad b_{j,k+\frac{1}{2}}:=\frac{1}{2}\left(b^{\rm N}_{j,k}+b^{\rm S}_{j,k+1}\right).$$

The procedure of solving (A8) is the same as the 1D case; see (Kurganov *et al.* 2020) for details.

Appendix 2. Well-balanced central-upwind numerical fluxes

We first introduce the central-upwind numerical fluxes from Chertock *et al.* (2018a), which are a slight simplification of the 2D central-upwind numerical fluxes rigorously derived by Kurganov and Lin (2007) using the integral form of the hyperbolic system of conservation laws

$$\begin{aligned}\mathcal{F}_{j+\frac{1}{2},k}=&\frac{a^+_{j+\frac{1}{2},k}\boldsymbol{F}\big(\boldsymbol{U}^{\rm E}_{j,k},Z_{j+\frac{1}{2},k}\big)-a^-_{j+\frac{1}{2},k}\boldsymbol{F}\big(\boldsymbol{U}^{\rm W}_{j+1,k},Z_{j+\frac{1}{2},k}\big)}{a^+_{j+\frac{1}{2},k}-a^-_{j+\frac{1}{2},k}}\\&+\frac{a^+_{j+\frac{1}{2},k}a^-_{j+\frac{1}{2},k}}{a^+_{j+\frac{1}{2},k}-a^-_{j+\frac{1}{2},k}}\left[\boldsymbol{U}^{\rm W}_{j+1,k}-\boldsymbol{U}^{\rm E}_{j,k}-\delta\boldsymbol{U}_{j+\frac{1}{2},k}\right],\\ \mathcal{G}_{j,k+\frac{1}{2}}=&\frac{a^+_{j,k+\frac{1}{2}}\boldsymbol{G}\big(\boldsymbol{U}^{\rm N}_{j,k},Z_{j,k+\frac{1}{2}}\big)-a^-_{j,k+\frac{1}{2}}\boldsymbol{G}\big(\boldsymbol{U}^{\rm S}_{j,k+1},Z_{j,k+\frac{1}{2}}\big)}{a^+_{j,k+\frac{1}{2}}-a^-_{j,k+\frac{1}{2}}}\\&+\frac{a^+_{j,k+\frac{1}{2}}a^-_{j,k+\frac{1}{2}}}{a^+_{j,k+\frac{1}{2}}-a^-_{j,k+\frac{1}{2}}}\left[\boldsymbol{U}^{\rm S}_{j,k+1}-\boldsymbol{U}^{\rm N}_{j,k}-\delta\boldsymbol{U}_{j,k+\frac{1}{2}}\right],\end{aligned}$$

where $\boldsymbol{U}^i_{j,k}$, $i\in\{\rm E,W,N,S\}$ are the point values of $\boldsymbol{U}$ at the corresponding four cell interfaces (see Appendix 1), $a^\pm_{j+\frac{1}{2},k}$ and $a^\pm_{j,k+\frac{1}{2}}$ are the one-sided local speeds of propagation in the x- and y-directions, respectively, given by (14)–(17). The terms $\delta\boldsymbol{U}_{j+\frac{1}{2},k}$ and $\delta\boldsymbol{U}_{j,k+\frac{1}{2}}$ represent the built-in

"anti-diffusion" and are computed by

$$\delta \boldsymbol{U}_{j+\frac{1}{2},k} = \text{minmod}\Big(\boldsymbol{U}^{\text{W}}_{j+1,k} - \boldsymbol{U}^{*}_{j+\frac{1}{2},k},\ \boldsymbol{U}^{*}_{j+\frac{1}{2},k} - \boldsymbol{U}^{\text{E}}_{j,k}\Big),$$
$$\delta \boldsymbol{U}_{j,k+\frac{1}{2}} = \text{minmod}\Big(\boldsymbol{U}^{\text{S}}_{j,k+1} - \boldsymbol{U}^{*}_{j,k+\frac{1}{2}},\ \boldsymbol{U}^{*}_{j,k+\frac{1}{2}} - \boldsymbol{U}^{\text{N}}_{j,k}\Big),$$

where the minmod function is applied in a component-wise manner, and the intermediate states $\boldsymbol{U}^{*}_{j+\frac{1}{2},k}$ and $\boldsymbol{U}^{*}_{j,k+\frac{1}{2}}$ are given by (see Kurganov and Lin 2007)

$$\boldsymbol{U}^{*}_{j+\frac{1}{2},k} = \frac{a^{+}_{j+\frac{1}{2},k}\boldsymbol{U}^{\text{W}}_{j+1,k} - a^{-}_{j+\frac{1}{2},k}\boldsymbol{U}^{\text{E}}_{j,k} - \Big[\boldsymbol{F}\big(\boldsymbol{U}^{\text{W}}_{j+1,k}, Z_{j+\frac{1}{2},k}\big) - \boldsymbol{F}\big(\boldsymbol{U}^{\text{E}}_{j,k}, Z_{j+\frac{1}{2},k}\big)\Big]}{a^{+}_{j+\frac{1}{2},k} - a^{-}_{j+\frac{1}{2},k}},$$
$$\boldsymbol{U}^{*}_{j,k+\frac{1}{2}} = \frac{a^{+}_{j,k+\frac{1}{2}}\boldsymbol{U}^{\text{S}}_{j,k+1} - a^{-}_{j,k+\frac{1}{2}}\boldsymbol{U}^{\text{N}}_{j,k} - \Big[\boldsymbol{G}\big(\boldsymbol{U}^{\text{S}}_{j,k+1}, Z_{j,k+\frac{1}{2}}\big) - \boldsymbol{G}\big(\boldsymbol{U}^{\text{N}}_{j,k}, Z_{j,k+\frac{1}{2}}\big)\Big]}{a^{+}_{j,k+\frac{1}{2}} - a^{-}_{j,k+\frac{1}{2}}}.$$

However, as shown in the 1D case by Kurganov *et al.* (2020), a direct application of the central-upwind numerical fluxes would not lead to a well-balanced scheme. We therefore follow Chertock *et al.* (2018a) and Kurganov *et al.* (2020) and switch a part of the numerical diffusion off when the solution is at or near the thermo-geostrophic equilibria. This leads to the following well-balanced modifications of the third and fourth components of the x-flux and second and fourth components of the y-flux, namely

$$\begin{aligned}
\mathcal{F}^{(3)}_{j+\frac{1}{2},k} &= \frac{a^{+}_{j+\frac{1}{2},k}p^{\text{E}}_{j,k}u^{\text{E}}_{j,k} - a^{-}_{j+\frac{1}{2},k}p^{\text{W}}_{j+1,k}u^{\text{W}}_{j+1,k}}{a^{+}_{j+\frac{1}{2},k} - a^{-}_{j+\frac{1}{2},k}} \\
&\quad + H\big(\psi_{j+\frac{1}{2},k}\big)\frac{a^{+}_{j+\frac{1}{2},k}a^{-}_{j+\frac{1}{2},k}}{a^{+}_{j+\frac{1}{2},k} - a^{-}_{j+\frac{1}{2},k}}\Big[p^{\text{W}}_{j+1,k} - p^{\text{E}}_{j,k} - \delta p_{j+\frac{1}{2},k}\Big], \\
\mathcal{F}^{(4)}_{j+\frac{1}{2},k} &= \frac{a^{+}_{j+\frac{1}{2},k}q^{\text{E}}_{j,k}b^{\text{E}}_{j,k} - a^{-}_{j+\frac{1}{2},k}q^{\text{W}}_{j+1,k}b^{\text{W}}_{j+1,k}}{a^{+}_{j+\frac{1}{2},k} - a^{-}_{j+\frac{1}{2},k}} \\
&\quad + H\big(\psi_{j+\frac{1}{2},k}\big)\frac{a^{+}_{j+\frac{1}{2},k}a^{-}_{j+\frac{1}{2},k}}{a^{+}_{j+\frac{1}{2},k} - a^{-}_{j+\frac{1}{2},k}}\Big[h^{\text{W}}_{j+1,k}b^{\text{W}}_{j+1,k} - h^{\text{E}}_{j,k}b^{\text{E}}_{j,k} - \delta(hb)_{j+\frac{1}{2},k}\Big], \\
\mathcal{G}^{(2)}_{j,k+\frac{1}{2}} &= \frac{a^{+}_{j,k+\frac{1}{2}}q^{\text{N}}_{j,k}v^{\text{N}}_{j,k} - a^{-}_{j,k+\frac{1}{2}}q^{\text{S}}_{j,k+1}v^{\text{S}}_{j,k+1}}{a^{+}_{j,k+\frac{1}{2}} - a^{-}_{j,k+\frac{1}{2}}} \\
&\quad + H\big(\psi_{j,k+\frac{1}{2}}\big)\frac{a^{+}_{j,k+\frac{1}{2}}a^{-}_{j,k+\frac{1}{2}}}{a^{+}_{j,k+\frac{1}{2}} - a^{-}_{j,k+\frac{1}{2}}}\Big[q^{\text{S}}_{j,k+1} - q^{\text{N}}_{j,k} - \delta q_{j,k+\frac{1}{2}}\Big], \\
\mathcal{G}^{(4)}_{j,k+\frac{1}{2}} &=, \frac{a^{+}_{j,k+\frac{1}{2}}p^{\text{N}}_{j,k}b^{\text{N}}_{j,k} - a^{-}_{j,k+\frac{1}{2}}p^{\text{S}}_{j,k+1}b^{\text{S}}_{j,k+1}}{a^{+}_{j,k+\frac{1}{2}} - a^{-}_{j,k+\frac{1}{2}}} \\
&\quad + H\big(\psi_{j,k+\frac{1}{2}}\big)\frac{a^{+}_{j,k+\frac{1}{2}}a^{-}_{j,k+\frac{1}{2}}}{a^{+}_{j,k+\frac{1}{2}} - a^{-}_{j,k+\frac{1}{2}}}\Big[h^{\text{S}}_{j,k+1}b^{\text{S}}_{j,k+1} - h^{\text{N}}_{j,k}b^{\text{N}}_{j,k} - \delta(hb)_{j,k+\frac{1}{2}}\Big].
\end{aligned}$$

The smooth cut-off function $H(\sigma)$ is defined as

$$H(\sigma)=\frac{(C\sigma)^m}{1+(C\sigma)^m},$$

where $C>0$ and $m>0$ are constants. In all of the presented simulations, we have used $C=400$ and $m=8$. Following Chertock *et al.* (2018a) and Kurganov *et al.* (2020), we take

$$\psi_{j+\frac{1}{2},k}=\frac{|K_{j+1,k}-K_{j,k}|}{\Delta x}\,\frac{x_{N_x+\frac{1}{2},k}-x_{\frac{1}{2},k}}{\max\left(|K_{j,k}|,|K_{j+1,k}|\right)},$$

$$\psi_{j,k+\frac{1}{2}}=\frac{|L_{j,k+1}-L_{j,k}|}{\Delta y}\,\frac{y_{j,N_y+\frac{1}{2}}-y_{j,\frac{1}{2}}}{\max\left(|L_{j,k}|,|L_{j,k+1}|\right)}.$$

Remark A.1: As in the 1D case, in order to accurately compute the point values $u^i_{j,k}$, $v^i_{j,k}$, $b^i_{j,k}$ and $b_{j,k}$ in the case if either $h^i_{j,k}$ or $\overline{h}_{j,k}$ is zero or very small ($i\in\{\mathrm{E},\mathrm{W},\mathrm{N},\mathrm{S}\}$), the same desingularisation technique used by Kurganov *et al.* (2020) has to be implemented. Furthermore, we apply a 2D version of "draining time step" technique from Bollermann *et al.* (2011) in order to guarantee the proposed central-upwind scheme preserves the positivity of the computed h and b.